

REPRESENTATION CHALLENGES
Augmented Reality and Artificial Intelligence in

Original

REPRESENTATION CHALLENGES

Augmented Reality and Artificial Intelligence in

Cultural Heritage and Innovative Design Domain / Giordano, A.; Russo, M.; Spallone, R.. - ELETTRONICO. - (2021), pp. 1-432.

Availability:

This version is available at: 11583/2927619 since: 2021-09-27T18:01:14Z

Publisher:

Franco Angeli

Published

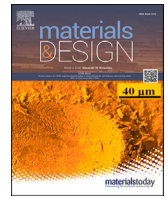
DOI:

Terms of use:



This article is made available under terms and conditions as specified in the corresponding bibliographic description in the repository

Publisher copyright

(Article begins on next page)



Mechanical design of lattice metamaterials: A multiscale homogenization-based operational procedure

Luca Cibrario ^{a, }, Chiara Gastaldi ^{a, }*, Cristiana Delprete ^a, Ivan Flaminio Cozza ^b

^a Politecnico di Torino, Department of Mechanical and Aerospace Engineering - DIMEAS, Corso Duca degli Abruzzi, 24, Torino, 10129, Italy

^b DUMAREY Automotive Italia S.p.A., Corso Castelfidardo, 36, Torino, 10129, Italy

ARTICLE INFO

Keywords:

Lattice structures
Multiscale
Numerical homogenization
De-homogenization
Additive manufacturing

ABSTRACT

Recent advancements in Additive Manufacturing technology have enabled the creation of components with innovative shapes, surpassing the limitations of conventional manufacturing methods. Lattice materials, also known as metamaterials, are a noteworthy example due to the possibility for effective control over mechanical and physical properties through the tuning of geometric parameters. One of the biggest limitations in the mechanical design and optimization of lattice-based structures is represented by the high computational time required in all the phases of numerical analyses due to their geometric complexity and the large number of repeated cells. The homogenization-based multiscale analysis is a computationally efficient numerical approach, able to extrapolate the macroscopic behavior of the lattice material from microscopic analyses. While the validity of homogenization to capture the displacement field has been proven in numerous studies, a comprehensive and operational procedure for the mechanical design of lattice metamaterials is absent in literature. Thus, the present paper introduces a methodology that couples micro and macroscale analyses to provide the essential mechanical data for design evaluation. Moreover, the proposed framework is rigorously validated on test cases through the comparison between the numerical data obtained from the homogenized component and its high-fidelity counterpart.

1. Introduction

In recent years, Additive Manufacturing (AM) has emerged as a revolutionizing technology enabling the production of complex shapes, that were once deemed impossible to be manufactured through traditional processes. Among these groundbreaking developments, lattice structures have gained significant attention for their unparalleled combination of strength, low weight, and highly customizable geometries [1,2]. Typical application of those revolutionary metamaterials includes lightweight structures, thanks to their high specific stiffness and strength [3–5], heat exchangers due to the large surface area, [6–9], energy absorbers due to the ability to sustain great deformation at a relatively low stress level [10–15], acoustic insulators [16,17] and biomedical applications [18–20].

Although Finite Elements Method (FEM) and Topology Optimization (TO) are well-established and powerful tools for the mechanical design of lattice metamaterials, numerical computations are often unfeasible due to the high computational time required to simulate even

small components accurately, given the large number of mesh elements needed to model their complex geometry [5,21–23]. In this context, the multiscale approach has emerged as a promising method to speed simulations up. It is based on homogenization, a numerical procedure able to retrieve the mechanical properties in the microscale of the smallest domain able to represent the behavior of the whole metamaterial, that is called Representative Volume Element (RVE). The equivalent mechanical properties can be used to model and simulate the whole lattice in the macroscale as a bulk material, allowing the generation of lighter meshes and, therefore, leading to a huge saving in computation time [24,25]. Homogenization was originally introduced to perform faster simulations of composite materials and several procedures have been developed since the end of the 20th century, ranging from analytical to numerical approaches. A comprehensive overview of homogenization algorithms can be found in Hassani et al. [25], Yan et al. [26], Barbero [27] and Somnic et al. [28].

Homogenization procedures based on numerical FE simulation are founded on the satisfaction of Hill-Mandel's theorem, that ensures the

* Corresponding author.

E-mail addresses: luca.cibrario@polito.it (L. Cibrario), chiara.gastaldi@polito.it (C. Gastaldi), cristiana.delprete@polito.it (C. Delprete), ivan_flaminio.cozza@dumarey.com (I.F. Cozza).

<https://doi.org/10.1016/j.matdes.2025.113614>

Received 13 November 2024; Received in revised form 3 January 2025; Accepted 13 January 2025

energetic consistency between the microscale real and homogenized models. From this requirement, three types of boundary conditions (BCs) can be employed to retrieve the equivalent mechanical properties: uniform boundary conditions (UBC) [29] either in form of traction or displacements, periodic boundary conditions (PBC) and enforced periodic boundary conditions (e-PBC), that are a combination of UBCs and PBCs [30]. Several algorithms, originally developed for the homogenization of composite materials, employing UBCs [31,32], PBCs [33–38] and e-PBCs [27], can be found in literature. Moreover, investigations on the effects of the different types of BCs and dimensions of RVEs on the outcomes of homogenization have been conducted. For example, Wang et al. [39] found that effective mechanical properties can be computed with high fidelity only through PBCs, while UBCs lead to window size and unit cell type-dependent results and, therefore, only apparent properties can be computed. However, effective and apparent mechanical properties tend to coincide as the dimensions of the RVE are big enough to minimize the effects of BCs.

Recently, homogenization has also been applied to lattice metamaterials to both evaluate their mechanical properties and develop fast performing TO frameworks. UBCs were employed in the investigation of strut-based lattice structures by Xu et al. [40], who found that the anisotropy of the structure is highly dependent on the spatial arrangement and dimensions of rods, and by Lohmuller et al. [41], that systematically estimated and compared stiffness constants and anisotropy of a large panel made of different unit cells, and for a large range of relative densities to find the best trade-off between stiffness and relative density. Al-Ketan et al. [42] investigated the architecture-property relationship associated with the possible configurations of a Triply Periodic Minimal Surface (TPMS) I-graph and wrapped package-graph (IWP) skeletal and sheet based lattice structure, and Lohmuller et al. [43] performed an extensive research on the mechanical properties of strut-based and TPMS lattice structures for the assessment of relationship between mechanical properties and relative density. However, recently PBCs have become the most used algorithm for the homogenization of lattice structures and examples of their use can be found in Bonatti et al. [44], who investigated the anisotropic elasticity, yield strength and specific energy absorption of strut-based and TPMS lattice structures as a function of the relative density, Chatzigeorgiou et al. [45], who compared various TPMS-based and strut-based lattices with respect to elastic properties, stiffness, anisotropy, and local stress distribution for biomedical implants, and Pais et al. [46], that concentrated on the evaluation of the mechanical properties of TPMS lattice structures and on the definition of a scaling law for Young's modulus and yield strength, to design optimized functionally graded structures for structural applications or reduced stress shielding in bio-applications.

Moreover, many TO-related papers, which employed homogenization to speed up numerical computations can be found in literature. In TO frameworks, homogenization is performed before the optimization cycle to create a map of the mechanical properties of unit cells, depending on relative density. After that, the optimization algorithm tries to find the optimal density in each point of the design volume and finally the lattice structure is generated. Li et al. [47] presented a TO framework constrained by manufacturability limits for the design of lattice components based on gyroids, Imediegwu et al. [48,49] presented a robust multiscale algorithm for the thermal and thermo-structural optimization of printable structures using lattice-based micro-architectures, Fernandes et al. [50] developed an experimentally-validated framework used to perform topology optimization of lattice structures subject to stress constraints, and Stromberg et al. [51] reported that optimization frameworks, which allow the creation of functionally graded lattice, lead to significantly stiffer solutions with respect to the corresponding optimal designs, made by using constant lattice densities.

Generally, in optimization workflows the fulfillment of mechanical design constraints, like yield or ultimate strength, is performed through the Finite Element Analysis (FEA) of the final optimized component. However, this implies a direct modeling and simulation of the full

macroscale lattice component, that, as it has been said previously, is computationally demanding and often unfeasible. Few studies, like Zhmaylo et al. [52], have proven the validity of the homogenized model to accurately simulate the real macroscale displacement of the full-scale model. However the development of a procedure, able to detect the critical zones within the homogenized lattice domain and compute the real stress field, would make the evaluation of each design within the optimization cycle more complete, as the design constraint on admissible stresses would be evaluated at each iteration.

Montoya-Zapata [53,54] presented a methodology that combines material homogenization and Design of Experiments (DoE) to estimate the stress-strain response in large lattice domains for lesser computational demands in comparison to FEA. DoE allows to estimate the stress-strain responses in large lattice domains and produces simple mathematical formulations to express the stresses in the lattice as functions of the displacements obtained through homogenization. The results on stress were reported to be not accurate enough, being the error in the order of 50-100%, and, therefore, that procedure should be used only for pre-evaluation designs. More recently, Coluccia et al. [55] presented an homogenization-based framework to estimate the fatigue life of strut-based lattice structures. It consists in the following steps: homogenization of the mechanical properties of the RVE, simulation of the full-scale homogenized model, identification of the most critical element through the evaluation of the homogenized strain field, and simulation of the critical cell to retrieve the maximum stress within the whole lattice domain. However, the procedure was not validated through comparison with a full-scale real model of the lattice component.

Taking inspiration from the above-mentioned procedure, this work not only builds upon it, but also expands the approach to include a rigorous selection of the homogenization procedure among those present in the literature. Additionally, the work involves a stringent validation against high-fidelity numerical benchmarks and highlights criticalities, that can only be identified when comparing the findings with high-fidelity numerical data. This comprehensive, unified, and validated operational multiscale homogenization-based workflow aims to provide fast and reliable FE simulations of lattice structures, delivering all the essential data necessary for the evaluation of component designs.

In Section 2, this work provides basic theoretical notions on the homogenization-based multiscale approach. In Section 3, the procedure for fast simulations of lattice structures is described. Section 4 is dedicated to comparing the performance of the homogenization schemes presented earlier in terms of computation time, convergence rate, and overall convenience to identify the most suitable algorithm. In Section 5, the fast multiscale procedure is applied to two case studies, and the results are compared to those obtained through full-scale Direct Numerical Simulation (DNS). Potential critical issues are highlighted, along with strategies to overcome them. Moreover in the appendixes, a more complete explanation of the mathematical equations behind the different homogenization approaches and their detailed implementation in FE codes are presented.

2. Homogenization-based multiscale modeling: an introduction

In this section few key theoretical notions about the multiscale approach, homogenization theory and algorithms are presented.

2.1. Multiscale modeling fundamentals

Multiscale modeling refers to an approach in which the mechanical response of the material is studied at one length scale, but the outcomes of the analysis are referent to several properties at another one [46]. Homogenization is a technique for evaluating the equivalent microscopic properties of a complex metamaterial with a periodic structure and it can be either performed through experiments or virtual tests based on numerical simulations. Being the FEA of entire lattice structures high demanding and often unfeasible due to the high number of mesh elements,

Table 1
Overview of the homogenization algorithms investigated in this work.

Algorithm	BCs	Notes	References
PBC Abs	PBC	⊕ Absolute node coupling to RPs	[58,27]
		⊖ Periodic mesh	
		⊖ Pre-process for node coupling	
PBC Rel	PBC	⊖ Periodic mesh	[58,34]
		⊖ Relative node coupling to RPs	
		⊖ Pre-process for node coupling	
PBC Interp	PBC	⊕ Generic mesh	[36,59]
		⊖ Complex pre-process for node coupling	
		⊖ Requires finer mesh	
Steven	UBC	⊕ Generic mesh	[31]
		⊕ Easy implementation	

numerical homogenization techniques have been developed and proven to lead huge time saving in the simulation of complex lattice structures composed of hundreds or even thousands of repeated unit cells [56].

The homogenization approach was born to model composites materials [36], but can be effectively used also for lattices: the dual fiber-matrix phase composition of composites is replaced with the solid and void phases in lattices. The final goal of the procedure is to transform a porous periodic lattice structure into an equivalent solid material with homogenized properties, that make it behave as if it were a true lattice domain [44]. A fundamental problem that has to be solved to effectively homogenize a lattice material is the definition of the minimum sufficient representative volume, so that the BCs effects are minimized. To address this issue the concept of RVE was introduced [57]. The RVE is a region much smaller than the entire lattice structure, it has the same mechanical characteristics and behavior as the lattice and its properties do not depend on BCs.

2.2. Homogenization: algorithms overview

In the literature, many different approaches for the homogenization of RVEs can be found. However, a thorough comparison of the performance of these algorithms on the same test case is lacking. In this work, the most commonly used methods have been implemented and tested to identify the best-performing one. In this section, four approaches employing UBCs and PBCs are presented. Additionally, a comparative overview is provided in Table 1, detailing the boundary conditions, pros and cons, and references for each algorithm.

PBCs with either relative or absolute coupling of nodes on opposite faces to reference points (RPs), which are used to apply the displacement BCs to the RVE, require periodic meshes. Those are special kind of meshes that have the nodes on opposite faces of the RVE in the same location. Creating periodic meshes is not always simple, because a dedicated meshing algorithm is required, especially in automated frameworks. Therefore, the formulation of PBCs with interpolation overcomes this issue by using a generic mesh and by interpolating the displacement of the virtual node on the opposite face from the surrounding ones, since it not guaranteed that two nodes located on two opposite faces of the RVE are in the same location. All the algorithms with PBCs require a pre-processing phase for the node coupling, that can be quite time consuming especially for larger meshes. Steven's algorithm relies on a reformulation of the classic implementation with UBCs to mimic the behavior of PBCs, and is a very simple and straightforward homogenization algorithm.

For deeper insights into the homogenization theory, algorithms and their detailed implementation the reader is referred to the appendixes.

3. The fast multiscale homogenization-based procedure

This section presents the complete workflow aimed at the simulation of lattice components composed of a high number of unit cells

repeated periodically throughout the domain space. The procedure presented in this work not only leads to a dramatic reduction in the overall computation time, but also provides detailed and accurate information about global displacement of the macroscopic component and microscopic stresses of the most loaded portions, allowing the designer to check the fulfillment of the mechanical integrity constraints. Moreover, the procedure is so efficient that makes the design of mechanical components with lattice domains feasible even on common laptops, available to researchers and engineers. For this study all the numerical computations were performed on a mobile workstation with 14 physical CPUs and 32 GB of RAM. A scheme of the workflow is depicted in Fig. 1.

The workflow relies on the homogenization-based multiscale approach, which allows the user not to model the entire lattice structure, but only few unit cells, that are used to retrieve all the needed information about the whole macroscopic model. As it will be presented in this section, the main phases are aimed at the retrieval of the behavior of the lattice through the homogenization of its RVE, the computation of the macroscopic displacements of the whole lattice structures using an equivalent bulk model, and finally the calculation of microscopic stresses in the most loaded zone through the FEA of critical cells.

Works like De Pasquale et al. [60], Moeini et al. [61], Stroemberg et al. [51] and Zhymalo et al. [52], proposed a partial multiscale workflow to retrieve the homogenized properties of the lattice RVE and compared the displacement results to those of numerical and experimental test on macroscopic lattice structures. On the contrary, this work was not only aimed at checking the validity of homogenization, but also at providing a complete and validated operational workflow to simulate efficiently and accurately large and complex lattice domains.

3.1. Phase 1: homogenization

The first phase of the workflow is in the microscale and consists in the computation of the equivalent properties of the lattice structure through homogenization. A convergence study on the RVE dimensions and those of the mesh element should be performed to get the effective homogenized elasticity tensor. It is convenient to start the convergence study from the smallest RVE composed of a single unit cell and a relatively coarse mesh. Then at each iteration the mesh element size should be reduced as long as the convergence on mesh size is achieved. Once the optimal mesh size is identified, the convergence study can be performed on the dimensions of the RVE. Thus, the first stage of the proposed workflow is a loop that consists in three different phases: modeling of the RVE through CAD tool, generation of the FE mesh using a proper meshing tool and application of the homogenization algorithm. The outcome of the first stage is the elasticity tensor of the homogenized lattice structure. From this moment on, the lattice domain can be replaced with an equivalent bulk material, that mechanically behaves like the original lattice structure.

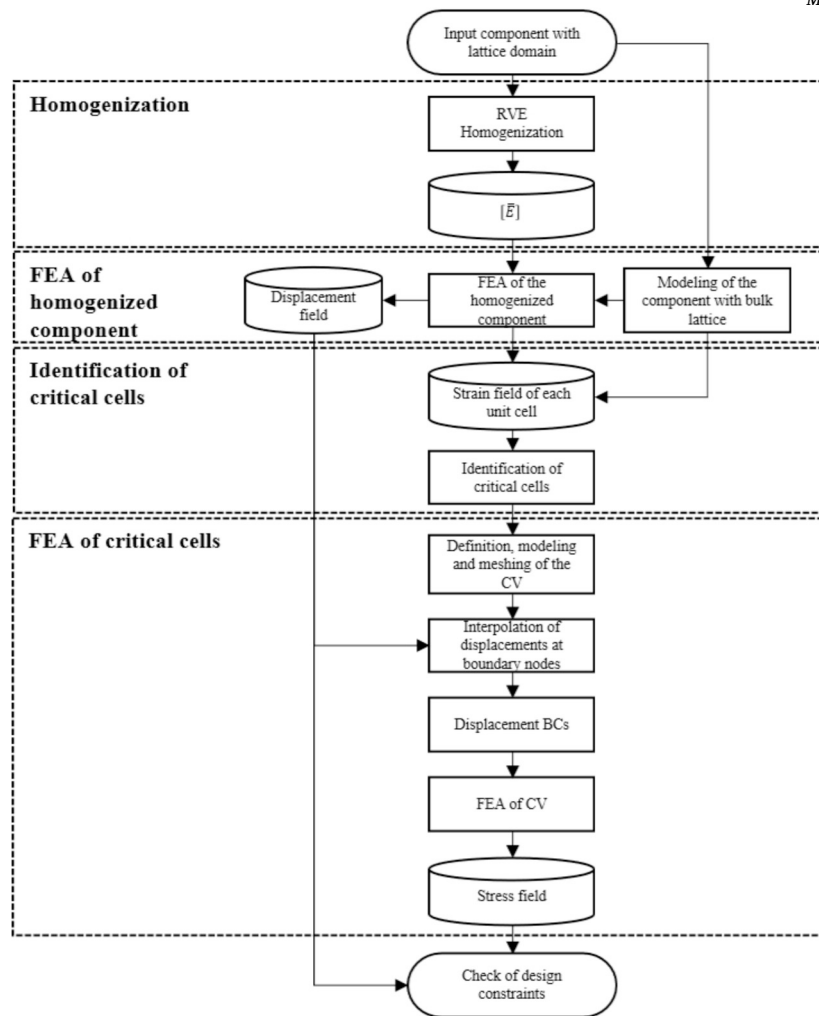


Fig. 1. Schematic layout of the multiscale procedure for the fast FEA of lattice structures.

3.2. Phase 2: FEA of the homogenized macroscopic component

In the second stage, the FE simulation of the macroscopic component is performed. The lattice domain is replaced by an equivalent bulk material to compute the real displacements. In the material assignment phase, the original constituent material has to be applied to all the bulk parts, while the homogenized equivalent material properties have to be applied to the lattice domain. Then the prescribed BCs in form of loads and displacements should be applied to the model and the simulation can be performed.

Once the numerical computation is completed, the macroscopic displacement field is available and corresponds to the real behavior of mechanical component under test, even in the lattice region. On the contrary, it is not possible to retrieve the real stress field for the lattice domain. Only a “mean” stress can be computed, because the equivalent bulk lattice domain does not present the original stress concentration areas. Therefore, at this stage it is still not possible to evaluate the fulfillment of the mechanical design constraints on stresses. However, even if the values of stress of the homogenized lattice and those of the real one do not match, the spatial distribution of the strain field is the same, i.e. the most stressed areas are the same.

3.3. Phase 3: identification of critical cells

The third stage of the workflow is aimed at the individuation of the most stressed cells of the lattice. Firstly, the geometrical topology of the

lattice domain has to be created. Cells are then divided into two categories: boundary cells and inner cells. The former group is composed of the cells that have at least one boundary face that is either free, i.e. not attached to any other cells or to the bulk material of the component. The latter group includes all the cells that are fully surrounded by other cells. This distinction is useful to analyze both the most stressed cells of the inner domain of the lattice and those that are at the interface with the bulk material, where high stresses are usually present due to the abrupt transition from solid to lattice. Then the homogenized strain at each integration point of the lattice domain, taken from the FEA of the homogenized component, is assigned to the cell to which the point under consideration belongs. Once all integration points have been processed, for each unit cell the mean and maximum Von Mises stress values are computed. Fig. 2 shows an insight on the steps related to the methodology presented in this section.

This allows to identify the most critical cells of each group, because the strain field is the measure of how large the deformation in a specific point is with respect to the undeformed state. Since the strain field is directly computed from the displacement field, that in the macroscopic homogenized simulation corresponds to the true displacement field of the real mechanical component, it represents the true “averaged” deformation of the real lattice. Therefore, the areas that are more deformed in the homogenized components are those that undergo the biggest deformations also in the real lattice domain and it is highly probable that will show the largest stresses in the final de-homogenization stage, where microscopic stresses are computed.

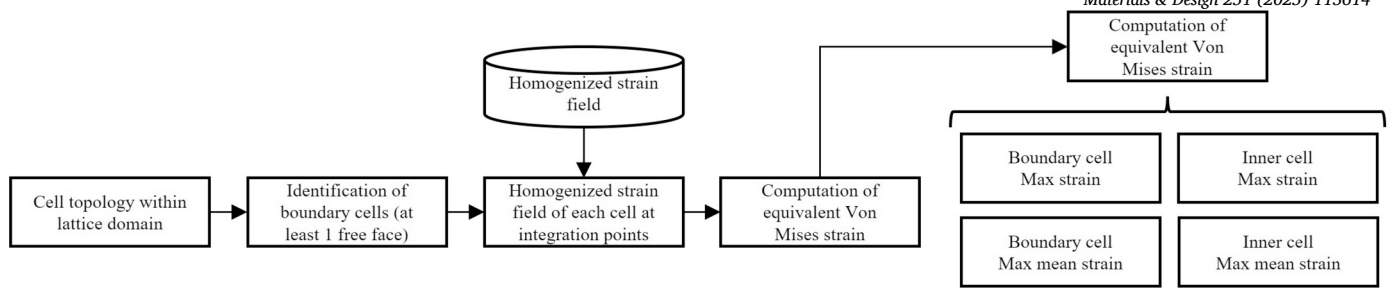


Fig. 2. Flowchart of the steps for the identification of the critical cells.

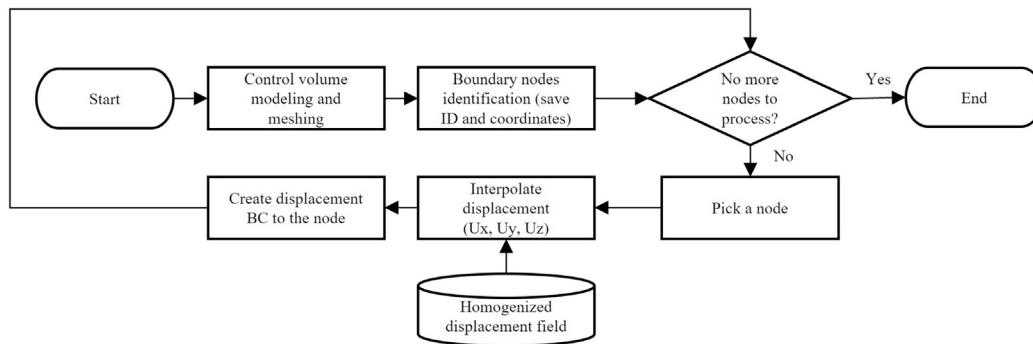


Fig. 3. Flowchart of the steps for the de-homogenization of the critical cells.

3.4. Phase 4: de-homogenization

The final stage of the workflow is dedicated to the de-homogenization and the retrieval of the microscopic stress field of the critical cells (see Fig. 3). The domain of each critical cell is modeled using CAD tools and meshed. The nodes that lie on each of the six boundary faces of the control volume are identified and their coordinates recorded. Then, the displacements along the three principal direction of each boundary node are computed through linear interpolation from the displacement field of the homogenized component and applied as displacement BCs. Once all boundary nodes have been processed, the microscopic stress field can be computed through FEA.

At this point, the workflow is concluded and all the relevant data for the check of the design have been computed. This procedure, as it can be seen from its description, allows the designer to avoid modeling and simulating the entire real component: the lattice domain is replaced with a solid one and just few cells are modeled and simulated. However the macro-displacement can be obtained as well as the real stresses of the most loaded zones. Moreover, they correspond to those that can be retrieved from a DNS of the full-scale component, but saving computation time.

4. Convergence study of homogenization algorithms on a strut-based lattice RVE

As presented in Section 2.1, multiscale FEA allows the simulation of large lattice domains exploiting information coming from the mechanical behavior in the microscale. Since periodic lattice structures are created through the repetition in space of the same unit cell, the first fundamental control volume that could be chosen to study the microscale mechanical properties should be the unit cell itself. However, homogenization on a single cell may suffer from boundary effects or may not represent the typical overall behavior of the whole lattice. Therefore, to get the true homogenized mechanical properties of the structure, a convergence study on the dimensions of the RVE must be performed: the algorithm is applied to RVEs composed of an increasing number of

unit cells along the three principal directions, as long as the entries of the elasticity tensor do not vary significantly anymore. Moreover, it is advisable to also conduct converge study on the dimensions of mesh elements.

In this section a comparison between the performances, the optimal RVE size and mesh dimensions for the four homogenization algorithms defined in Sections 2.2, is presented. The goal was the evaluation of the best trade-off between the accuracy of results and the computation time to retrieve the effective components of homogenized elasticity tensor. The study was conducted on a lattice composed of strut-based tetra cells, which are obtained by combining standard cubic and BCC unit cells, with side length $L = 6$ mm and beam thickness $t = 0.75$ mm. The base material of the lattice was the aluminum alloy AlSi10Mg, modeled as an isotropic material with the following properties $E = 70$ GPa and $\nu = 0.33$. The design of the RVE was performed using a totally open-source tool developed by the authors in Python. The RVE was then meshed with quadratic tetrahedral elements, using the free software Gmsh [62]. The setup of the FE model as well as the post processing activities for each iteration of the homogenization procedure were performed using self-developed Python scripts able to create the input file for the FE open-source software CalculiX and analyze its output [63]. For convenience sake, only two out of the six simulation were performed on each RVE (tension load along x and shear load in xy plane). In fact the tetra cell behavior can be modeled as an orthotropic material, that can be characterized using only the three variables C_{11} , C_{12} and C_{44} , as explained in Appendix A.2.1.

Figs. 4a, 4b and 4c report the results of the convergence study on the components of the homogenized elasticity for an increasing number of elements per cell and for RVE composed of 1, 8 and 27 cells. As it can be clearly seen, Steven's homogenization and PBCs show almost flat trend in dependence of the increasing number of mesh elements and RVE dimensions, being the parameters of the homogenized elasticity tensors almost constant. The results about PBCs with interpolation are not reported in the plot, because they showed the worst behavior and needed more than 200000 elements per unit cell to converge to the results of the other algorithms. Fig. 4d reports the mean computation time

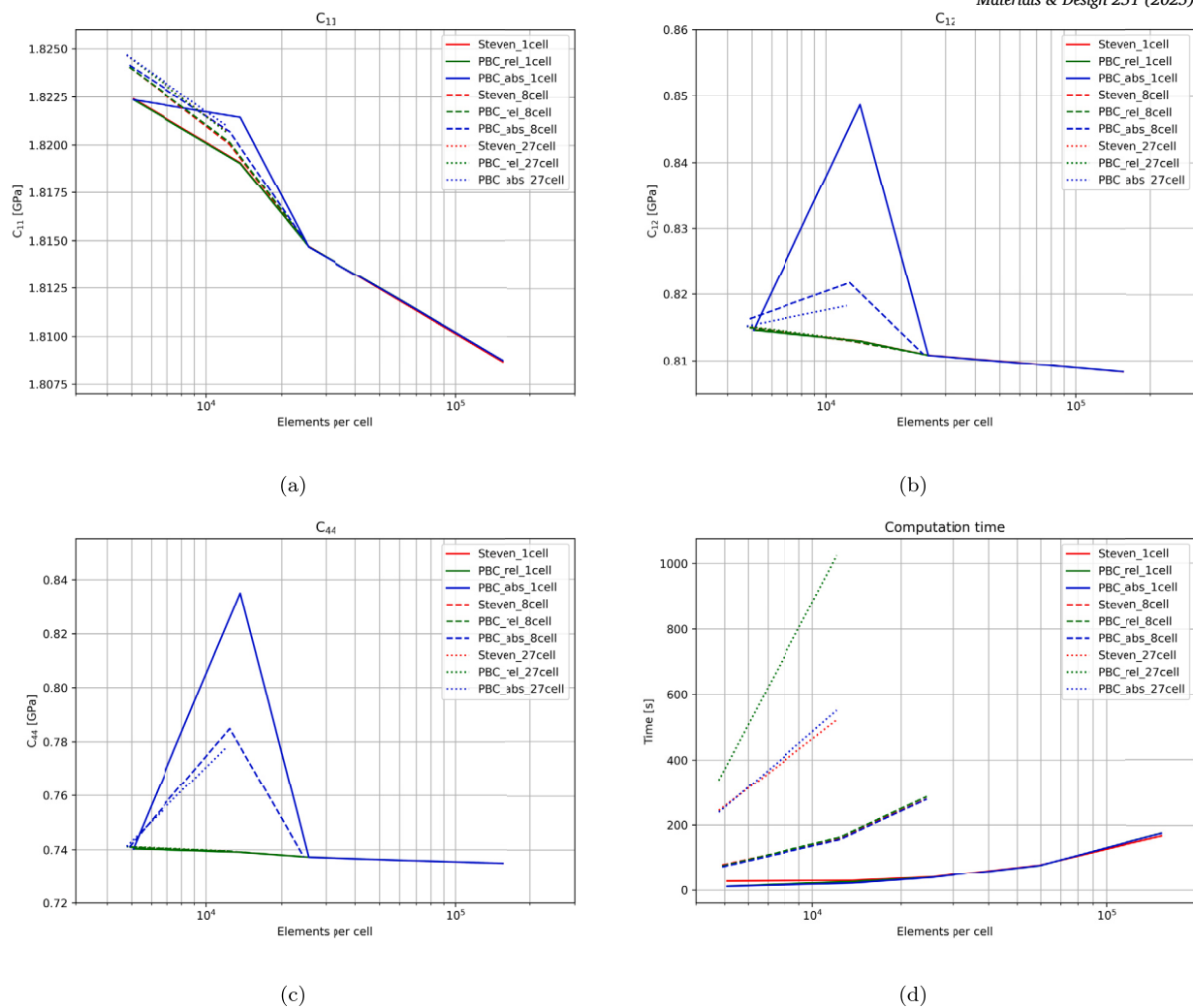


Fig. 4. Results of the convergence study on the C_{11} (a), C_{21} (b), C_{44} (c) components of the homogenized elasticity tensor, and overall computation time (d).

per iteration. It can be seen that Steven's homogenization algorithm is faster than PBCs, considering that in this comparison the pre-processing time to setup MPCs between coupled nodes is not considered. The algorithm with PBCs and interpolation takes even longer pre-processing time, making it computationally unfeasible.

Since Steven's algorithm provided the same results as PBCs, while saving little computation time, it was selected as the best performing homogenization algorithm, being also very simple and straightforward to be implemented. Moreover, for the implementation of PBCs it is always required a periodic conformal mesh, that in many cases it is not easy to obtain: some CAE software like Simulia Abaqus and Altair Optistruct have some dedicated functions, but they can only be performed manually, preventing the inclusion of the homogenization algorithm in automated procedures.

From the whole convergence study, it was noticed that for the tetra cell the variation on elasticity tensor parameters in dependence of RVE and mesh size was under 1% in almost all the investigated cases. On the contrary, the increase in mean computation time per simulation, which has to be multiplied for the number of FEA employed in the whole homogenization algorithm to get the total computation time, was not negligible. In most of cases a one-cell RVE with at least 30000 mesh elements could be enough to get the precise homogenized behavior of the lattice structure. Further refinement on both RVE and mesh size would only have increased the computation time, without getting significant improvements on outcomes.

5. Results and discussion

This section presents the application of the complete procedure for the efficient and fast FEA of lattice structures, presented in Section 3, to two sample case studies of interest for our industrial partners, denoted as Case A and Case B. The aim of the study was the numerical computation of the macroscopic displacements and stresses of the most critical zones of the lattice under static loading, that represent the most important data for the mechanical design of components. Results were also compared to the outcomes of the DNS of real lattice components to prove the validity of the presented method. Through the presented analyses, the work aims to provide hints and recommendations to save as much computation time as possible, while getting reliable results. In fact there are particular situations in which special care is needed.

5.1. Case A: cantilever beam with reinforcing lattice domain

The mechanical component under study is a beam made of AlSi10Mg aluminum alloy with a reinforcing prismatic lattice domain composed of tetra cells. The two specimens analyzed in this research are depicted in Fig. 5 and their geometrical parameters are summarized in Table 2. The beam has got dimensions $100 \times 24 \times 12.5$ mm, while the back plate has got side dimensions 50×40 mm and its thickness is 5 mm. Defining the major the cathetus of the lattice domain directed along the length of the beam as x and the other one as k , the lattice volume can be defined solving the system of equations:

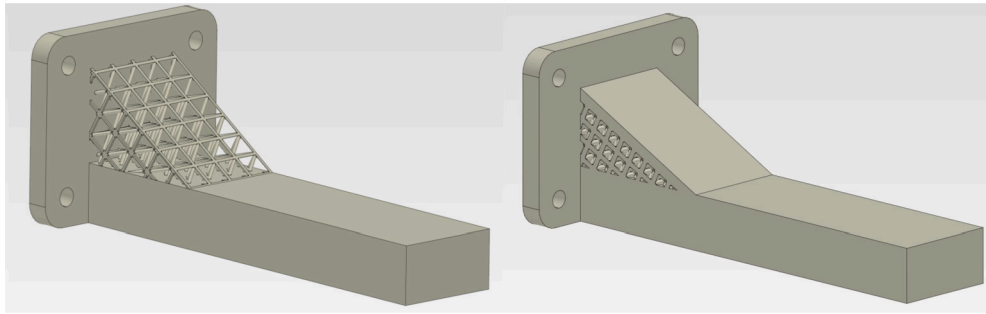


Fig. 5. CAD model of Beam A (left) and Beam B (right).

Table 2

Geometric parameters of the lattice beams.

Parameter	Beam A	Beam B
Cell Type	Tetra	Tetra
Cell dimensions (L)	6 mm	4 mm
Beam thickness (t)	0.75 mm	1.25 mm
Skin	0 mm	Top 20 mm
x/k	1.6	2.0

Table 3

Mechanical and simulation data of the optimal RVE for cubic cell.

Homo parameters	Beam A	Beam B
Homogenization algorithm	Steven	Steven
RVE size	$2 \times 2 \times 2$ cells	$2 \times 2 \times 2$ cells
Mesh size	0.2 - 0.3 mm	0.25 - 0.35 mm
C_{11}	1.81 GPa	17.2 GPa
C_{12}	0.811 GPa	6.80 GPa
C_{44}	0.731 GPa	6.15 GPa

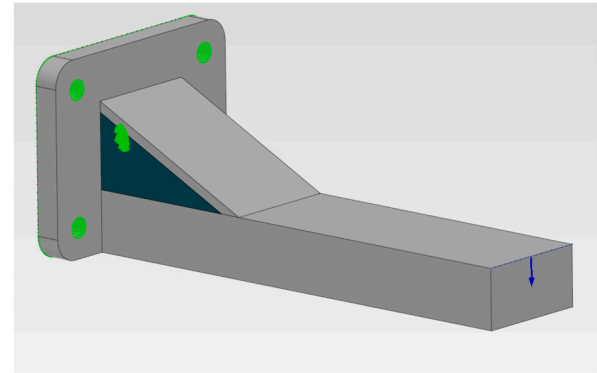


Fig. 6. FE model of Beam B.

Fig. 6 depicts the FE model setup of the homogenized Beam B. The boundary conditions applied to all the models were the same: a 500 N load on the tip of the beam and a fixed displacement boundary condition applied to the back of the plate and the four holes. The boundary conditions that were applied to both the homogenized models, where the lattice domain was replaced by the equivalent bulk material, and the full-scale model, meant to be solved through DNS, consisted in a concentrated load of 500 N on the nodes at the tip of the beam pointing downwards in the direction orthogonal to the axes of the beam itself, producing a bending effect. In addition, a fixed boundary condition constraint, locking all the translational and rotational degrees of freedom, was applied to all the nodes of the back face of the plate and those belonging to the four holes.

The lattice and bulk domains of full-scale components were modeled through a single solid FE model and the mechanical properties of the AlSi10Mg aluminum alloy were assigned to it ($E = 70$ GPa, $\nu = 0.33$). On the contrary, the FE model of the homogenized components consisted of two solid models, the former related to the external bulk frame made of AlSi10Mg and the latter belonging to the homogenized lattice domain. The two solid domains were linked together through a tie constraint to make them behave as a unique component. The homogenized bulk material of the lattice domain was modeled as an orthotropic material, that requires the definition of the nine components of its elasticity tensor. As already said, the RVEs studied in this work showed an orthotropic behavior with cubic symmetry, meaning that only three constants are required to be fully characterized. Therefore for the definition of all the mechanical constants required by the FE software, we remind that $C_{11} = C_{22} = C_{33}$, $C_{12} = C_{23} = C_{13}$, $C_{44} = C_{55} = C_{66}$.

The comparison between the displacement field of the real and homogenized beams for Beam A and Beam B is reported in Figs. 7 and 8, respectively, while Table 4 reports the displacement values at their tip, that was selected as a control point.

The comparison between the real and homogenized displacement confirms that the displacement field of the homogenized beam reflects the true deformation of the real one. However, as already said, the stress

$$\begin{cases} x \cdot k = 1250 \text{ mm}^2 \\ x/k = a \end{cases} \quad (1)$$

where a is defined in Table 2.

The mechanical component is restrained on the back plate and a force of 500 N is applied on the tip of the beam. The base constituent aluminum alloy was modeled as an isotropic elastic material with the following mechanical properties $E = 70$ GPa, $\nu = 0.33$.

5.1.1. Homogenization

In Appendix A.2.1 strut-based cells like the tetra cell can be modeled as orthotropic materials with cubic symmetry. Thus, the elastic constitutive law of the material can be described using only the three independent parameters: the in-plane elastic constant C_{11} , out-of-plane elastic constant C_{12} and shear component C_{44} . This allows the full characterization of the homogenized material by performing only two out of the six simulations.

Once the homogenization algorithm has been selected, a convergence study on both mesh size and RVE dimensions was conducted to compute the effective mechanical properties of the lattice. Data on the homogenized mechanical properties of the lattice structures under test, the selected homogenization algorithm, as long as the size of the best trade-off mesh size and RVE dimensions are summarized in Table 3.

5.1.2. FEA of macroscopic component and computation of real displacement field

This section is dedicated to the FEA of the macroscopic mechanical component under test. Both the real and homogenized beams were simulated to compare results and prove the validity of homogenized simulations. FE model setup and numerical computations were performed using the open source software PrePoMax, that contains pre- and post-processing functionalities for the open source solver CalculiX.

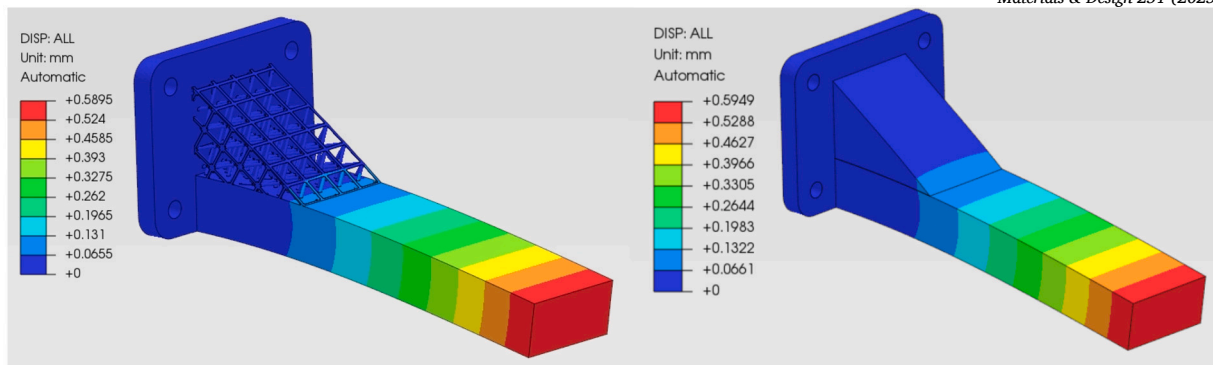


Fig. 7. FEA displacement results of the real (left) and homogenized beams (right) of Beam A.

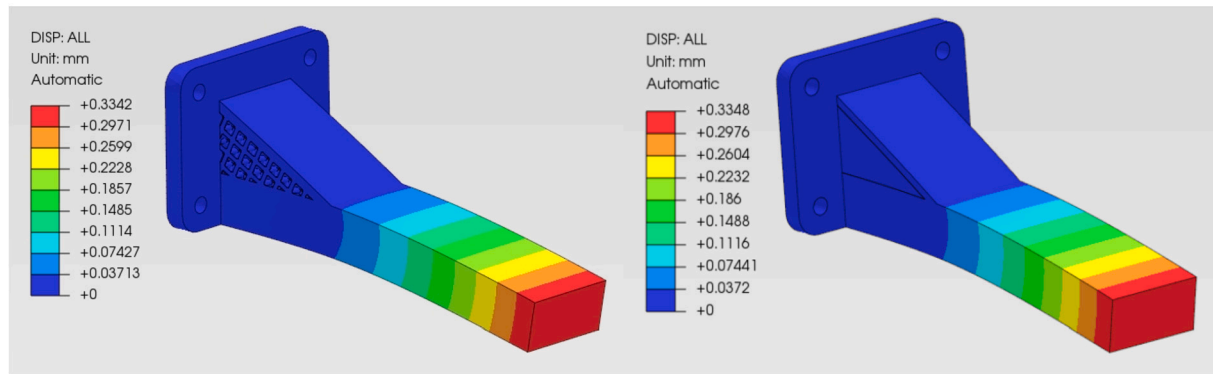


Fig. 8. FEA displacement results of the real (left) and homogenized beams (right) of Beam B.

Table 4
Comparison between real and homogenized displacement and stress data for Beam A and Beam B beams.

	Displacement data					
	Beam A			Beam B		
	Real	Homo	Difference [%]	Real	Homo	Difference [%]
Max disp. [mm]	0.59	0.59	0.0	0.33	0.33	0.0
Disp. at tip [mm]	0.59	0.59	0.0	0.33	0.33	0.0
Max stress [MPa]	268	3.78	-98	118	10.3	-91
Computation time	2.5 hrs	20 s	-99.9	3 hrs	35 s	-99.7

field of the homogenized model does not reflect the true behavior of the lattice domain, because the equivalent bulk material does not present any stress concentration area. Therefore, a de-homogenization on the most critical cells of the lattice is required.

5.1.3. Identification of critical cells and computation of real stress field

As it can be seen in Fig. 9, from the analysis of the homogenized strain field the most critical zones of the real lattice component can be effectively identified. The strain values at each integration point were stored and assigned to the cell the integration point belonged to, and the most critical cells were identified as those with the highest maximum strain. In this study it was decided to rely on Von Mises strain, which is an equivalent value of all the strain components. It is defined as follows:

$$\epsilon_{VM} = \frac{2}{3} \frac{1}{\sqrt{2}} \sqrt{(\epsilon_x - \epsilon_y)^2 + (\epsilon_y - \epsilon_z)^2 + (\epsilon_z - \epsilon_x)^2 + 6\epsilon_{yz}^2 + 6\epsilon_{zx}^2 + 6\epsilon_{xy}^2} \quad (2)$$

Fig. 10 shows the Von Mises strain field of the homogenized lattice domains in Beam A and Beam B. The red zones represent the most

stressed areas and it is likely that the most critical cells fall into those regions.

Once the critical cells had been identified, they could be simulated to compute the real stress field. In both cases, the critical cells were located in the red zones depicted in Fig. 10. Two different approaches were followed for the FEA microscale model: the former consisted in the simulation of the critical cell only, while the latter involved the simulation of a control volume centered in the Center of Gravity (CoG) of the critical cell but with larger side dimension. That was done to reduce the boundary effects induced by the application of displacement BCs. Each control volume, centered in the CoG of the critical cells, was modeled, meshed and a FE model was setup. The same material of the real lattice component, AlSi10Mg, was assigned to the model. As presented in Section 3, displacement BCs were applied to each node of the control volume lying on the boundary surfaces. Displacement values along the three principal directions were retrieved from the homogenized simulation results and the displacement values at each boundary node of the control volume model were computed through linear interpolation. Then, they were applied to the FE model through single point displacement constraints. Finally, simulation was performed and data of the stress field within the critical cell were stored. Tables 5 and 6 report the comparison between

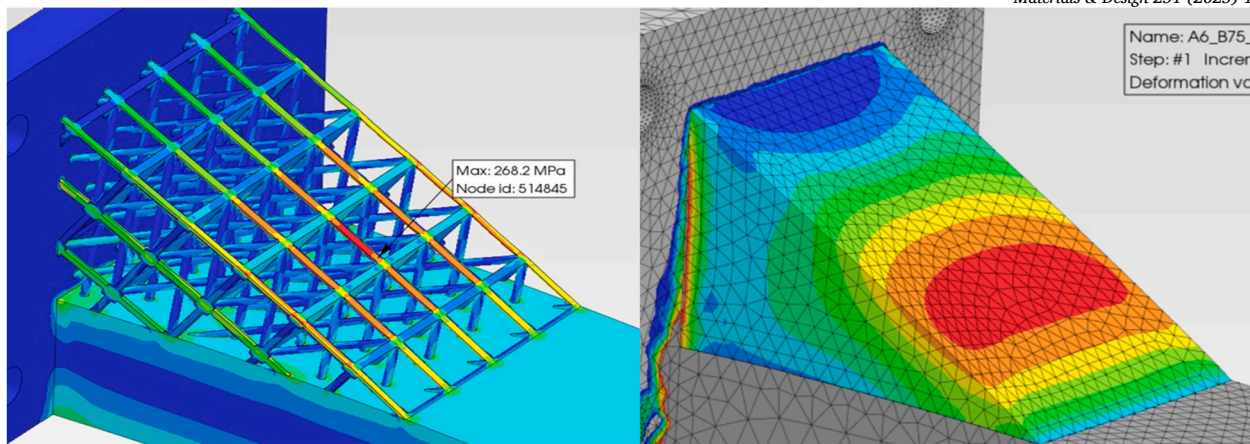


Fig. 9. Real stress field (left) and homogenized strain (right) field of Beam A.

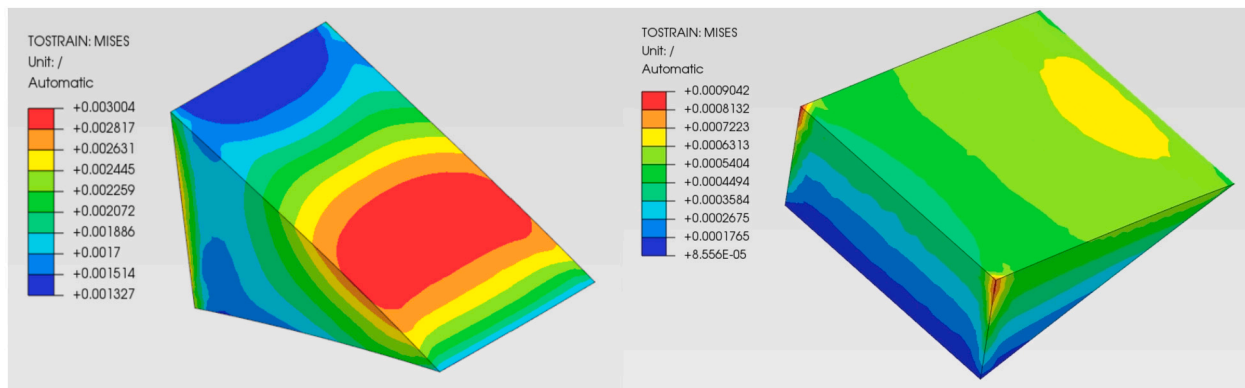


Fig. 10. Strain field of the homogenized lattice domain in Beam A (left) and Beam B (right).

Table 5
Comparison between real and homogenized stress data of Beam A.

Stress data - Beam A							
Control volume side length	1 cell			1.5 cells		3 cells	
	Real	Homo	Err [%]	Homo	Err [%]	Homo	Err [%]
Max stress [MPa]	268	320	19	294	10	278	4
Mean stress [MPa]	29.0	66.4	129	46.5	60	30.4	5
SD [MPa]	25.3	50.3	99	44.0	74	25.9	2

the maximum, mean and standard deviation (SD) stress values within the most critical cell.

The de-homogenization algorithms correctly identified the critical cells in both cases as those with the maximum value of the homogenized Von Mises strain. In Case A the most critical point was located in the central portion of the upper free surface of the lattice domain. On the contrary, in Case B the corner at the interface between the bulk plate, upper skin and lattice domain was the weakest. As it can be seen from Table 5 reporting microstress data for Beam A, the figures obtained through de-homogenization get closer to real ones, as the control volume becomes bigger. In fact, this reduces the effects of the displacement BCs applied to its boundary and the behavior of the microscale lattice is closer to that obtained through DNS. Moreover, the mean stress and its standard deviation become even more precise. A slightly different trend was observed in Beam B, whose de-homogenization results are reported in Table 6. In this case, a too big control volume led to an increasing error on the maximum stress and to an underestimation of the mean stress field.

The previously presented numerical data were also validated experimentally. A beam with the same geometric characteristics as Beam

A was designed and produced through AM technology, using the aluminum alloy employed in the numerical simulations (AlSi10Mg). Three different specimens were realized and tested under a bending load applied to the tip of the beam. The BCs used in the numerical analyses were replicated in the experimental tests: the beam was fastened to the testing machine with screws through the holes in the base and an increasing load was applied to its tip until the complete failure of the specimen. The load cells and displacement sensors located at the tip of the beam were used to record force and displacement data. Through the analysis of experimental results, stress data obtained through the multiscale procedure were validated with maximum error within 5%.

Further investigations on the de-homogenization of internal non-critical cells revealed that the results were really close to the real one even with smaller control volumes. In fact, as it was reported by Yan et al. [26], in the homogenization process the RVE is subjected to uniform or periodic BCs. Thus, the homogenized model is generally not suitable for RVE subjected to high stress gradient on the boundary: rapid changes of the stress states could compromise the procedure of volume averaging from which the effective moduli are derived. However, high stress gradient usually decays rapidly from the stress riser, such as the stress

Table 6
Comparison between real and homogenized stress data of Beam B.

Stress data - Beam B							
Control volume side length	1 cell			1.5 cells		3 cells	
	Real	Homo	Err [%]	Homo	Err [%]	Homo	Err [%]
Max stress [MPa]	118	118	0	125	5.9	130	11
Mean stress [MPa]	13.3	10	-25	10.6	-20	7.9	-41
SD [MPa]	10	9.9	-1	9	-10	7.9	-21

concentration areas at the strut joints or at the bulk-lattice interface. Moreover, the following guidelines were proposed:

- The boundary of the selected region of interest should be sufficiently away from the high stress gradient zone, and the macro stresses on the region's boundary can vary only mildly;
- The center element in which the micro fields remain exact must be placed well within the region's boundary.

The former point is motivated by the fact that homogenization is a material characterization technique, which imposes a deformation state in the unit cell under test, that mimic its behavior when it is immersed in an infinitely big lattice. Therefore, the homogenized properties are not suitable for the simulation of models with very high deformation and stress conditions only located in small portions of the model: the higher the extension of the high stress or displacement gradient areas, the worse the results of the homogenized simulation could be, especially in those regions. As already said, an example of a high stress gradient zone could be the interface between the bulk and lattice domains. Moreover, contact zones between the lattice and another part of the mechanical component could be critical areas, where the homogenized model could not perfectly reflect the behavior of the real one.

The reason behind the former point was highlighted by the analysis of results presented previously: the imposition of displacement boundary conditions at each node, lying on the boundaries of the control volume, introduces some boundary effects, which induce high stresses near those areas. However, those non-physical values rapidly decay and here the need for control volumes bigger than one unit cell arises.

The two points raised by Yan et al. are a good explanation of the need for bigger control volumes to get good results and for the better behavior in the inner portions of the lattice domains. By simulating control volumes with side length of about 2 cells, sufficiently good results can be obtained with a small computation effort. Moreover, the results of the de-homogenization of Beam B seem to have a different trend with respect to Beam A, because the critical cell, which is located at the upper corner of the lattice and at the interface with the skin and the back plate, corresponds to a fraction and not to a complete cell. Therefore, the homogenization cannot be precise in those cases and strange behavior may rise.

It should also be pointed out, that the microstress values computed through de-homogenization were reported to be always higher than the real ones, making this procedure safe-oriented. The presented approach can be effectively employed in optimization algorithms, where a fast evaluation of a high number of designs is required. In fact, optimization frameworks for lattice structures without a valid method to speed up simulations are addressed as almost unfeasible, or at least really expensive. As a rule of thumb, to get reliable results with errors lower than 10%, that could be compensated with a safety factor, it is advisable to simulate control volume with side length of at least 1.5 cells.

5.2. Case B: lattice plate

The second specimen under test consisted in a lattice plate composed of $8 \times 8 \times 3$ cubic cells with side dimension $L = 50$ mm and beam thickness $t = 10$ mm, surrounded by a bulk frame. The material is the AlSi10Mg aluminum alloy with the same mechanical properties as in

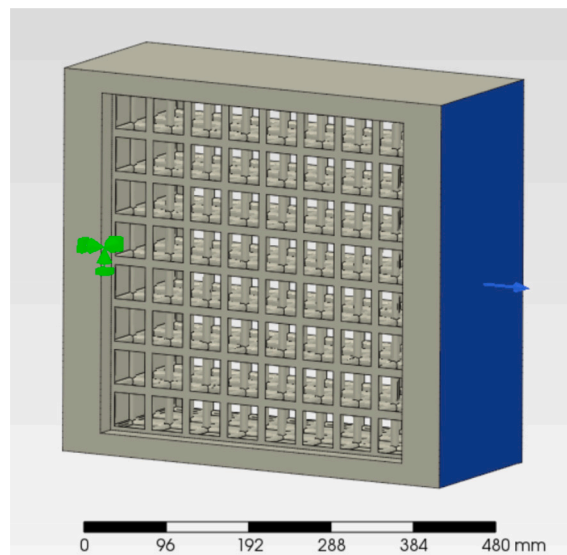


Fig. 11. FE model of the lattice plate with traction load along the x axis.

Case A (see Section 5.1). A fixed BC was applied to all the nodes of the back face of the frame (along x direction), locking all their degrees of freedom. In Plate A a uniform surface load of 500 kN along the x axis was applied to the opposite face of the frame, while in Plate B a total bending force of 50 kN was applied to the same face, but pointing downwards along the y direction. The model is depicted in Fig. 11.

First the cubic unit cell was homogenized using the Steven's algorithm. Also in this case the cubic cell behavior can be modeled through an orthotropic material with cubic symmetry. After the convergence study on mesh and RVE size the equivalent material properties were identified as $C_{11} = 2350$ MPa, $C_{12} = 137$ MPa, and $C_{44} = 45.4$ MPa.

At this point, the FEA of the macroscopic real and homogenized plates could be performed, following the procedure explained in the previous sections. The comparison between the results obtained through DNS and those of the homogenized model is presented in Fig. 12 for the traction Plate A and in Fig. 13 for the bending Plate B.

Finally the de-homogenization phase was done in order to find the most loaded cells and retrieve the highest stress values. Fig. 14 depicts the Von Mises stress field for the plate in Plate A and Plate B. The most critical cells were identified in correspondence of the red zones in both cases. Again it was verified that the interface between the lattice and the bulk frame is the weakest area due to the stress concentration effects.

The trend on the results of the de-homogenization phase was nearly the same as the previous test case presented in Section 5.1. Again a control volume with side length of about 2 cells was identified as the best solution to get a maximum error on the maximum stress lower than 10%. As already said, in both Plate A and Plate B, the critical cells are not in the central area of the lattice domain, but at the interface with the bulk. Therefore, the results suffer from boundary effects, and the perfect adherence between real and de-homogenized stress cannot be achieved.

This test case was presented to point out two operational concepts, that have to be taken into account when one want to use the procedure presented in this work.

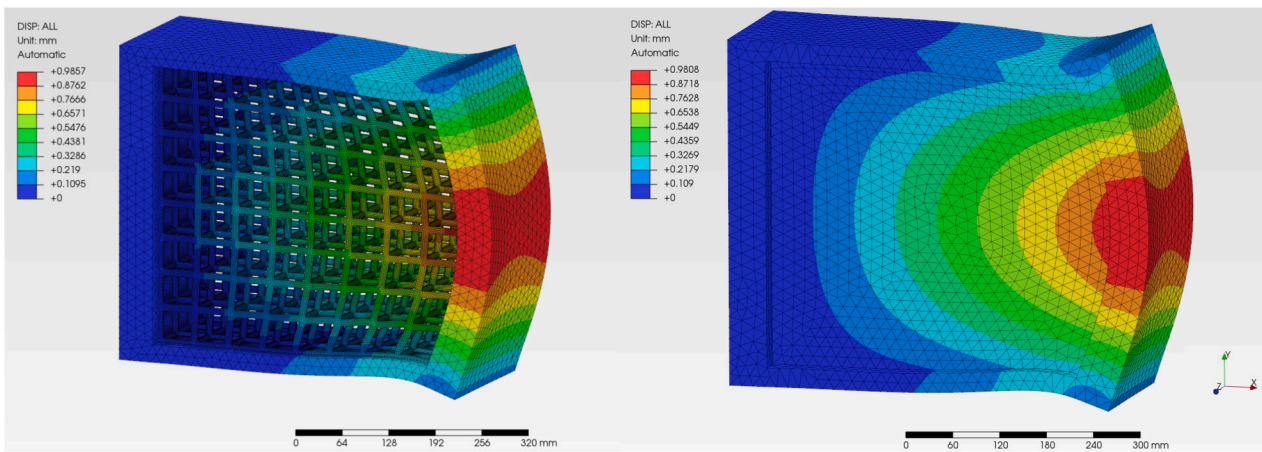


Fig. 12. Comparison between the displacement results of the real (left) and homogenized (right) lattice plate in the traction loading case.

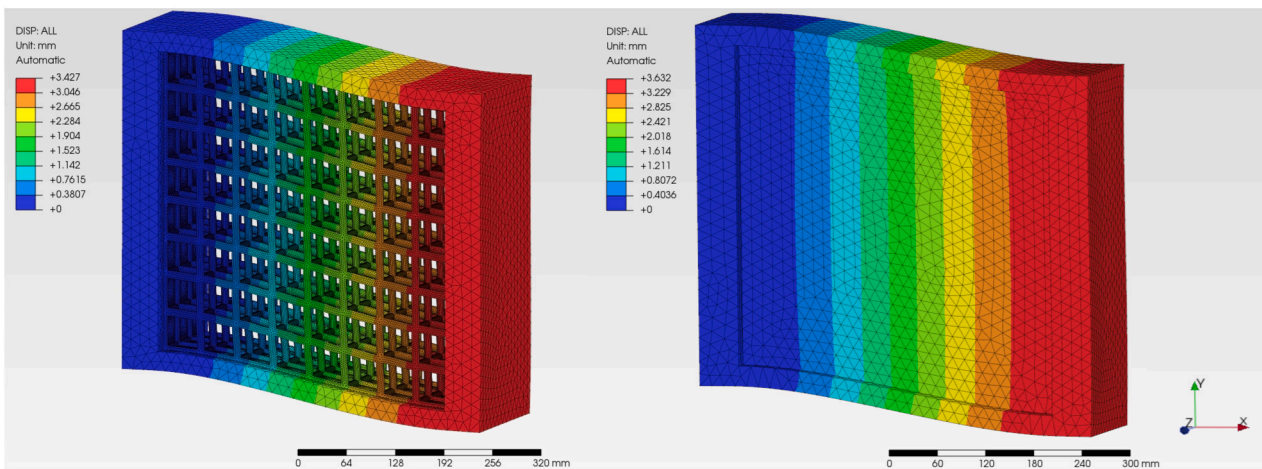


Fig. 13. Comparison between the displacement results of the real (left) and homogenized (right) lattice plate in the traction loading case.

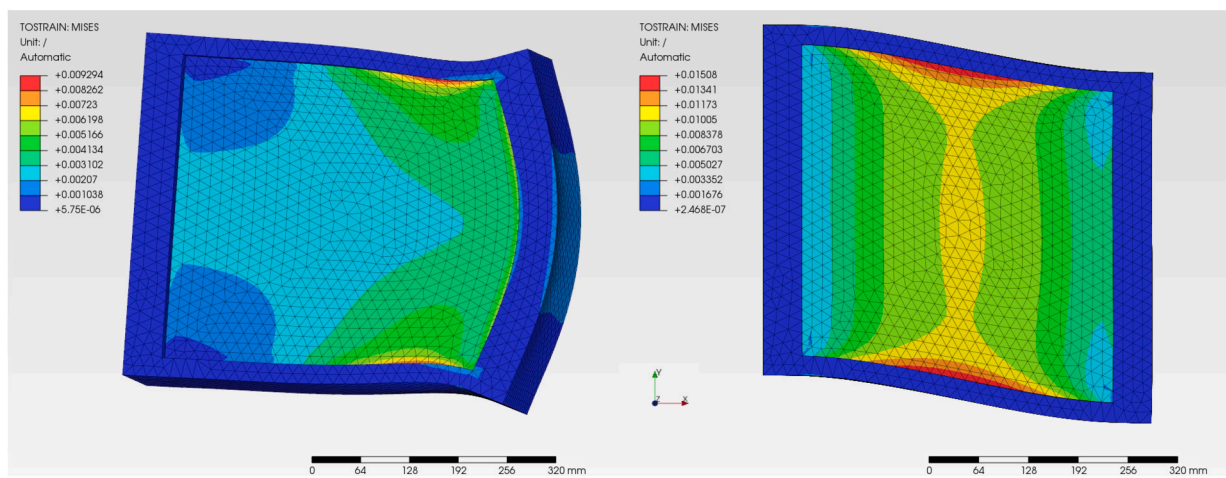


Fig. 14. Homogenized Von Mises strain field for Plate A (left) and Plate B (right).

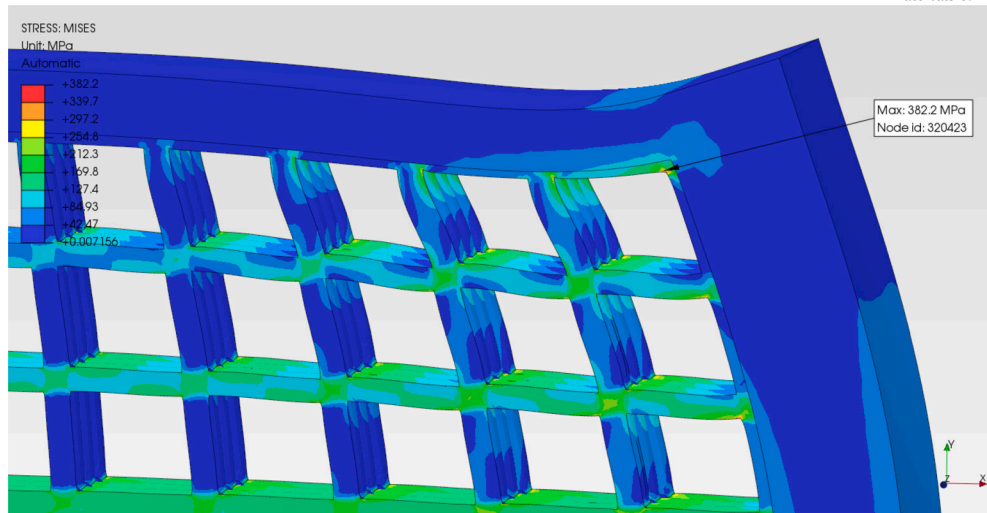


Fig. 15. Highlight of the true maximum stress point in Plate A with traction load.

- Identification of critical cells: in Plate A, the most critical cell was identified as that centered in the upper red zone, because it showed the maximum absolute and mean value of homogenized strain within its domain (see Fig. 14). However, the maximum real stress was located inside the adjacent cell, located in the upper corner of the lattice domain (see Fig. 15). Its maximum absolute and mean homogenized strains were very close to those of the true critical cell, however, the double interface with the bulk external frame caused a stronger stress concentration zone and, thus the rise of the highest stress values within the whole lattice. Therefore, it is advisable to simulate the cells that have multiple interfaces with bulk portions, when the maximum homogenized strain area is close to them. In this way, one is sure to have found the true maximum microstress of the lattice.
- Homogenization-related issues: as it can be seen from Fig. 13, the results on the macroscopic displacement field, obtained through the homogenized model, are farther to those of the DNS with respect to all other cases presented in this work. In this case the error on the maximum macroscopic displacement is around 5%. This discrepancy is related to the way in which cells are deformed by the imposed load in the macroscopic simulation and the deformation modes allowed by the homogenization procedure. In fact, in the standard homogenization, the RVE is subjected to two main loading conditions: pure traction/compression stretch and pure shear deformation. For that reason, the results on macroscopic displacement of Plate A (see Fig. 12), where a pure traction load is imposed are almost perfect. Also in both the test cases presented in Section 5.1, homogenized macroscopic displacement matched the true ones, even if a bending load was imposed. This could be linked to the way the cells are deformed. In fact, due to the orientation of the cells of the lattices with respect to the direction of deformation of the whole mechanical components, the deformation mode of each cell was very close to a pure traction. On the other hand, in Plate B presented in this section, cells are deformed in a way that is not provided by homogenization. Two solutions are proposed to overcome this issue e further reduce the error on macroscopic displacement.
 - Bigger lattices: the BCs imposed to the RVE during homogenization simulate its behavior as if there were an infinite repetition of the control volume in each direction. Thus as the lattice domain becomes bigger, the unit cells tend to be deformed in a way more similar to that simulated during the homogenization procedure. As a consequence, the results of the FEA on the homogenized macroscopic component get more accurate. Plate B with bending load had only 8 cells along the main directions of

deformation, so a higher number of cells would have led to better results.

- Second-order homogenization: several loading conditions, such as pure bending or torsion, especially when applied to lattices composed of quite small number of cells, induce states of deformations also dependent to higher-order effects at smaller scales, that cannot be captured by the standard homogenization procedure. Second-order computational homogenization schemes offer a more complete description of the behavior of lattice metamaterials at the cost of higher computational time and a dedicated FE framework (the so-called FE^2 architecture), that is generally not implemented in standard FEA software. In fact, the accuracy of the model is enhanced by incorporating the second gradient elasticity model, that requires the handling of the strain gradient and second order stresses both in the micro and macroscale model. Basic theoretic notions on second-order elasticity can be found in Mindlin's works [64,65], while more information on this topic along with the formulation of the microscale homogenization model and way to handle the macroscopic simulations can be found in Kouznetsova et al. [66,67], Weeger [68], Rodrigues Lopes et al. [69] and Dos Santos et al. [70].

6. Conclusions

Lattice structures offer significant potential due to their exceptional mechanical properties, lightweight nature, and the ability to finely tune their behavior for specific applications. However, their numerical design and optimization have been strongly constrained by the extensive computation time required at every phase of Direct Numerical Simulation (DNS). To address this challenge, this research work aimed to develop an operational procedure, that significantly reduces the overall computation time, while still providing all the necessary data for evaluating the mechanical designs.

In this study, a multiscale framework based on homogenization was presented and tested on specific case studies, allowing a thorough comparison between the results obtained through homogenization and those from DNS. The use of homogenized properties enabled a reduction in simulation time for mechanical components with lattice domains by over 99%, while the macroscopic displacement field closely matched that of DNS. However, because the stress field did not accurately reflect the true behavior of the lattice, a de-homogenization process was necessary. The critical cells within the lattice domain were identified by analyzing the homogenized strain field, and these cells were then simulated by applying the homogenized displacement to the boundary

nodes. It was observed that the error in maximum stress between the de-homogenized critical cell and DNS decreases as the control volume involved in submodeling increases, minimizing boundary effects.

As demonstrated by the results presented in this section, the multiscale framework, introduced in this work, enables the integration of simulations across different length scales, leveraging the strengths and extracting maximum information from each scale. The process begins at the microscale, which, while computationally efficient, provides insights only into the characteristic mechanical behavior of the lattice cells, independent of the specific loading and boundary conditions of the analyzed component. Subsequently, the macroscale is addressed, incorporating the homogenized information obtained from the microscale to evaluate the overall mechanical response of the studied component under its actual boundary conditions. Finally, the analysis returns to the microscale to focus on the critical cells, that are those subjected to the highest stresses, allowing for the determination of peak stress values.

This approach avoids the need for full-scale, high-fidelity simulations of the entire component, but provides all the data necessary for a comprehensive mechanical evaluation of the design. It delivers the macroscopic displacement field, which has implications for interactions with neighboring components, and the critical stress values, essential for assessing whether the maximum yield or failure loads have been exceeded.

Two families of critical cells were evaluated: those located near the bulk-lattice interface and those in the lattice core. For each family, cells experiencing both the average and maximum homogenized deformation were analyzed. This enables the investigation of various critical scenarios where the true maximum internal lattice stress might occur. It is well known that regions near the bulk-lattice interface are prone to high stress due to abrupt geometric transitions. Furthermore, the framework addresses cases where the deformation is either highly localized or more uniformly distributed across the entire cell.

This research contributes uniquely by providing, to the best of the authors' knowledge, the only complete comparison between different homogenization algorithms, evaluated both in terms of methodology and performance on a specific test case. Additionally, a rigorous validation of the multiscale framework against a high-fidelity simulation is presented, a contribution missing from previous literature works. The proposed procedure has proven to be reliable and effective in reducing computation time, making it suitable for integration into optimization frameworks, where it can evaluate each design in just a few seconds. Future research will focus on extending this procedure to study the dynamic response of mechanical components with lattice domains.

CRedit authorship contribution statement

Luca Cibrario: Writing – original draft, Visualization, Validation, Software, Conceptualization. **Chiara Gastaldi:** Writing – review & editing, Supervision, Project administration, Methodology, Investigation, Funding acquisition, Conceptualization. **Cristiana Delprete:** Writing – review & editing, Supervision, Methodology, Funding acquisition. **Ivan Flaminio Cozza:** Writing – review & editing, Supervision, Project administration, Methodology.

Declaration of competing interest

The authors declare that they have no known competing financial interests or personal relationships that could have appeared to influence the work reported in this paper.

Acknowledgements

The authors are grateful for the invaluable scientific and technical advice provided by Giuseppe Credo, Mario Saracino, and the entire Dumarey team. Their expertise and support were instrumental in guiding the research and improving the quality of our work.

Appendix A. Notes on homogenization

In this appendix some deeper insights into the homogenization theory and the derivation of the mathematical equations, which allow the computation of the effective homogenized properties, are presented.

A.1. Hill-Mandel principle

Sub-scale modeling is energetically consistent, only if the deformation energy at the macroscopic level is equal to the volume average of the microscale stress work: at any equilibrium state of the RVE, characterized by the stress field σ and the strain field ϵ , the following equation must be satisfied [59]:

$$\bar{\sigma}_{ij}\bar{\epsilon}_{ij} = \frac{1}{V_{RVE}} \int_V \sigma_{ij}\epsilon_{ij} dV \quad (\text{A.1})$$

where $\bar{\sigma}$ and $\bar{\epsilon}$ are the average stress and strain tensors, V_{RVE} is the total volume of the RVE and the indexes i, j represent the principal directions.

The average stress and strain tensors are defined as [71]:

$$\begin{aligned} \bar{\sigma}_{ij} &= \frac{1}{V} \int_V \sigma_{ij} dV \\ \bar{\epsilon}_{ij} &= \frac{1}{V} \int_V \epsilon_{ij} dV. \end{aligned} \quad (\text{A.2})$$

In absence of body forces, using the averaging theory Eq. (A.2) and the equilibrium condition of the RVE, i.e. $\nabla \cdot \sigma = 0$, the Hill-Mandel principle Eq. (A.1) can be rewritten in the more convenient form:

$$\oint_{\partial V} (t_i - \bar{\sigma}_{ij}n_j)(u_i - \bar{\epsilon}_{ik}x_k) dS = 0 \quad (\text{A.3})$$

where t and u are the traction and displacement at the boundary of the RVE, x and n are the coordinate and the normal of the surface dS where the integral is currently evaluated.

The Hill condition Eq. (A.3) guarantees that the effective modulus of the RVE, calculated by energy and direct approaches, is the same. It is satisfied by four different types of BCs:

- *Dirichlet or kinematic* (displacement controlled)

$$u_i = \epsilon_{ij}^0 x_j \quad (\text{A.4})$$

- *Neumann or natural* (traction controlled)

$$t_i = \sigma_{ij}^0 n_j \quad (\text{A.5})$$

- *Mixed*, obtained through the combination of Eqs. (A.5) and (A.4)

$$(t_i - \sigma_{ij}^0 n_j)(u_i - \epsilon_{ij}^0 x_j) = 0 \quad (\text{A.6})$$

- *Periodic boundary conditions (PBCs)*

$$u_i(x + L) = u_i(x) + \epsilon^0 L \quad (\text{A.7})$$

$$t_i(x + L) = -t_i(x) \quad (\text{A.8})$$

where σ_{ij}^0 and ϵ_{ij}^0 are the uniform applied stress and strain, respectively, and L is the dimension of the RVE in the i -th direction. In Eq. (A.6) only one component of t_i or u_i is specified at a time on a given surface. It has to be pointed out that Dirichlet and Neumann BCs are both kinds of UBCs.

Applying the average stress theorem under traction boundary conditions (Eq. (A.5)), the average stress $\bar{\sigma}_{ij}$ is equal to the applied stress

$$\begin{aligned} \sigma_{ij}^0 \\ \bar{\sigma}_{ij} = \sigma_{ij}^0 \end{aligned} \quad (\text{A.9})$$

while applying the average stress theorem under displacement boundary conditions (Eq. (A.4)), the average strain $\bar{\varepsilon}_{ij}$ is equal to the applied (uniform) strain ε_{ij}^0

$$\bar{\varepsilon}_{ij} = \varepsilon_{ij}^0 \quad (\text{A.10})$$

The strain energies predicted by the different boundary conditions must satisfy the following inequality, if the average strain ε_{ij}^0 for each case is assumed to be the same:

$$U^\Sigma \leq U^P \leq E^E \quad (\text{A.11})$$

where U^Σ, U^P, E^E are the strain energy predicted by homogeneous traction boundary conditions, periodic boundary conditions, and homogeneous displacement boundary conditions, respectively.

It is clear that the homogeneous displacement boundary conditions overestimate the effective moduli whereas the homogeneous traction boundary conditions underestimate them. It should also be pointed out that the application of the homogeneous displacement boundary conditions generally would not guarantee to produce a periodic boundary traction. Similarly, the application of the homogeneous traction boundary conditions would not guarantee the displacement periodicity at the boundaries.

A.2. Computation of the homogenized elasticity tensor

The determination of the effective mechanical properties of the lattice metamaterial is performed through an iterative procedure that requires the application of six independent loading conditions to the RVE. This study focused on the study of UBCs and PBCs both in term of displacement constraints. Thus, each loading condition consists in a specific displacement field with all but one null entries of the strain tensor.

Recalling the Hooke's law in matrix form

$$\{\sigma\} = [E]\{\varepsilon\} \quad (\text{A.12})$$

where $\{\sigma\}$ and $\{\varepsilon\}$ are the stress and strain tensors, respectively, and $[E]$ is the stiffness matrix of the material, the goal of homogenization is the computation of the 21 unknown independent constants, thanks to the symmetry of the off-diagonal entries, of the homogenized stiffness tensor:

$$[\bar{E}] = \begin{bmatrix} \bar{C}_{11} & \bar{C}_{12} & \bar{C}_{13} & \bar{C}_{14} & \bar{C}_{15} & \bar{C}_{16} \\ \bar{C}_{21} & \bar{C}_{22} & \bar{C}_{23} & \bar{C}_{24} & \bar{C}_{25} & \bar{C}_{26} \\ \bar{C}_{31} & \bar{C}_{32} & \bar{C}_{33} & \bar{C}_{34} & \bar{C}_{35} & \bar{C}_{36} \\ \bar{C}_{41} & \bar{C}_{42} & \bar{C}_{43} & \bar{C}_{44} & \bar{C}_{45} & \bar{C}_{46} \\ \bar{C}_{51} & \bar{C}_{52} & \bar{C}_{53} & \bar{C}_{54} & \bar{C}_{55} & \bar{C}_{56} \\ \bar{C}_{61} & \bar{C}_{62} & \bar{C}_{63} & \bar{C}_{64} & \bar{C}_{65} & \bar{C}_{66} \end{bmatrix} \quad (\text{A.13})$$

Taking for example the first iteration of the procedure, whose homogenized deformation state is

$$\{\bar{\varepsilon}\} = \{\bar{\varepsilon}_{11}, 0, 0, 0, 0, 0\}^T, \quad (\text{A.14})$$

plugging it into Eq. (A.12), it is possible to compute one column of the homogenized elasticity tensor at a time:

$$\{\bar{\sigma}_{11}, \bar{\sigma}_{22}, \bar{\sigma}_{33}, \bar{\sigma}_{12}, \bar{\sigma}_{23}, \bar{\sigma}_{31}\}^T = \bar{\varepsilon}_{11} \{\bar{C}_{11}, \bar{C}_{22}, \bar{C}_{33}, \bar{C}_{12}, \bar{C}_{23}, \bar{C}_{31}\}^T \quad (\text{A.15})$$

Repeating the analysis five more times will produce all the required terms of the homogenized elasticity matrix. Following this procedure, diagonal terms are calculated twice, but such redundancy can be used to provide a crude but useful indicator of the accuracy of the simulations.

After the simulation of each loading case, the output data are used to compute the homogenized mechanical properties of the lattice material. It is assumed that the average mechanical properties of the RVE are equal to those of the real component as a consequence of Mendel-Hill theorem. By manipulating the Hill-Mandel theorem (Eq. (A.1)) and

assuming the only non-zero component of the imposed strain field of each iteration $\bar{\varepsilon}_{ij} = 1$, three main approaches can be followed for the post-processing of the simulation of each loading case, to compute the entries of the homogenized elasticity tensor.

- *Reaction forces*: stresses $\bar{\sigma}_{ij}$ are computed from the reaction forces at the boundaries at the RVE

$$\bar{\sigma}_{ij} = \frac{F_{ij}}{S_i} = \bar{C}_{ij} \quad (\text{A.16})$$

where F_{ij} is the total reaction force on the RVE face S_i with normal in the i -direction and along the j -direction.

- *Stresses*: the average stresses are directly computed from the microscale stresses within the RVE

$$\bar{\sigma}_{ij} = \frac{1}{V_{RVE}} \sum_{e=1}^{n_e} \sum_{I=1}^{n_{int}} \sigma_{ij}(\mathbf{r}_I) w(\mathbf{r}_I) J(\mathbf{r}_I) = \bar{C}_{ij} \quad (\text{A.17})$$

where n_e is the number of element of the mesh, n_I is the number of integration points of each element, w , J and \mathbf{r} are the weight, determinant of the jacobian and position of the integration point I , respectively, and V_{RVE} is the total volume of the bounding box containing the RVE.

- *Energy*: the entries of the elasticity tensor are directly computed from the sum of the microscale energy stored inside the RVE

$$\bar{C}_{ij} = \frac{2U}{V_{RVE}} \quad (\text{A.18})$$

where U can be computed through one of these three equivalent equations:

$$U = \sum_{e=1}^{n_e} U_e V_e$$

$$U = \frac{1}{2} \sum_{e=1}^{n_e} \sum_{I=1}^{n_{int}} \sigma^T(\mathbf{r}_I) \varepsilon(\mathbf{r}_I) w(\mathbf{r}_I) J(\mathbf{r}_I) \quad (\text{A.19})$$

$$U = \frac{1}{2} \sum_{e=1}^{n_e} \sum_{I=1}^{n_{int}} \varepsilon^T(\mathbf{r}_I) C \varepsilon(\mathbf{r}_I) w(\mathbf{r}_I) J(\mathbf{r}_I)$$

where U_e is the element energy density and V_e is the volume of the mesh element.

A.2.1. Effective mechanical properties of the homogenized unit cell

Strut-based and TPMS-based can be modeled as orthotropic materials with cubic symmetry. Thus, the elastic constitutive law of the material can be described using only the three independent parameters C_{11} , C_{12} and C_{44} . The stiffness matrix is the following form:

$$[\bar{E}] = \begin{bmatrix} \bar{C}_{11} & \bar{C}_{12} & \bar{C}_{12} & 0 & 0 & 0 \\ \bar{C}_{12} & \bar{C}_{22} & \bar{C}_{12} & 0 & 0 & 0 \\ \bar{C}_{12} & \bar{C}_{12} & \bar{C}_{33} & 0 & 0 & 0 \\ 0 & 0 & 0 & \bar{C}_{44} & 0 & 0 \\ 0 & 0 & 0 & 0 & \bar{C}_{44} & 0 \\ 0 & 0 & 0 & 0 & 0 & \bar{C}_{44} \end{bmatrix} \quad (\text{A.20})$$

Components \bar{C}_{11} and \bar{C}_{12} are related to the tensile/compressive behavior of the lattice material, while \bar{C}_{44} is responsible for the shear behavior. Sometimes, it is useful to relate the mechanical behavior of the homogenized lattice material to the following engineering constants [43,45]:

$$E^* = \frac{\bar{C}_{11}^2 + \bar{C}_{11}\bar{C}_{12} - 2\bar{C}_{12}^2}{\bar{C}_{11} + \bar{C}_{12}} \quad (\text{A.21})$$

$$\nu^* = \frac{\bar{C}_{12}}{\bar{C}_{11} + \bar{C}_{12}} \quad (\text{A.22})$$

$$G^* = \bar{C}_{44} \quad (\text{A.23})$$

Table B.7
Nodal displacement BCs for the six load cases.

Displacement boundary conditions						
Node coordinates	Case 1	Case 2	Case 3	Case 4	Case 5	Case 6
$x = -L_x/2$	$\epsilon_x = 0$	$\epsilon_x = 0$	$\epsilon_x = 0$	$\epsilon_y = 0$	$\epsilon_x = 0$	$\epsilon_z = 0$
$x = L_x/2$	$\epsilon_x = 1$	$\epsilon_x = 0$	$\epsilon_x = 0$	$\epsilon_y = 0.5$	$\epsilon_x = 0$	$\epsilon_z = 0.5$
$y = -L_y/2$	$\epsilon_y = 0$	$\epsilon_y = 0$	$\epsilon_y = 0$	$\epsilon_x = 0$	$\epsilon_z = 0$	$\epsilon_y = 0$
$y = L_y/2$	$\epsilon_y = 0$	$\epsilon_y = 1$	$\epsilon_y = 0$	$\epsilon_x = 0.5$	$\epsilon_z = 0.5$	$\epsilon_y = 0$
$z = -L_z/2$	$\epsilon_z = 0$	$\epsilon_z = 0$	$\epsilon_z = 0$	$\epsilon_z = 0$	$\epsilon_y = 0$	$\epsilon_x = 0$
$z = L_z/2$	$\epsilon_z = 0$	$\epsilon_z = 0$	$\epsilon_z = 1$	$\epsilon_z = 0$	$\epsilon_y = 0.5$	$\epsilon_x = 0.5$

where E^* , G^* and ν^* are the effective Young’s modulus, shear modulus and Poisson’s ratio, respectively.

The degree of anisotropy of the unit cell can be evaluated through the Zener ratio Z , that is defined as [41,72]:

$$Z = \frac{2\bar{C}_{44}}{\bar{C}_{11} - \bar{C}_{12}} \tag{A.24}$$

When $Z = 1$ the unit cell has an isotropic behavior, $Z > 1$ means that the predominant contribution of the \bar{C}_{44} component makes the structure suitable for shear, while $Z < 1$ means that the structures possesses a predominant tensile/compression behavior [73].

Appendix B. Homogenization: algorithms and implementation

In this appendix the detailed explanation of each homogenization algorithm described in Table 1 as long as the way to implement them in FE codes is presented.

B.1. Steven’s homogenization algorithm

Steven [32,31] presented an easy and straightforward procedure to compute the effective elastic properties of composite materials, that can also be used for lattice metamaterials [40,43,41,53,54,52]. This algorithm relies on a reformulation of UBCs to mimic PBCs in symmetric RVEs and uses reaction forces to compute the entries of the elasticity tensor.

Table B.7 resumes the nodal displacement BCs regarding the translational Degrees of Freedom (DoFs) that have to be applied to the RVE in the six simulation cases. In addition, all the rotational DoFs are always locked.

In the first case, the BCs are defined as follows:

$$\begin{aligned} \Delta l_x|_{x=L_x/2} &= \bar{\epsilon}_{11} L_x \\ \Delta l_x|_{x=-L_x/2} &= \Delta l_y|_{y=-L_y/2} = \Delta l_y|_{y=L_y/2} = \Delta l_z|_{z=-L_z/2} = \Delta l_z|_{z=L_z/2} = 0 \end{aligned} \tag{B.1}$$

where Δl is the deformation between the initial and final position.

Even though in the original algorithm proposed by Steven, the entries of the homogenized elasticity tensor are computed through the reaction forces at the boundary of the RVE, however any of the approaches presented in Appendix A.2 can be used.

B.2. Homogenization with periodic boundary conditions

The other approach for the homogenization of the RVE, which satisfies the Hill-Mendel principle, consists in the imposition of PBCs. There are some researches in literature reporting that it can predict better equivalent mechanical properties with respect to UBCs [74,75,39,37,36].

Considering a periodic RVE with volume V , its boundaries δV can be decomposed into two opposing parts δV^+ and δV^- such that, $\delta V = \delta V^+ \cup \delta V^-$ and $\delta V^+ \cap \delta V^- = \emptyset$. If kinematic PBCs are applied to the RVE, the displacements on a pair of nodes located on opposite boundary faces of δV are:

$$u_i^{j+} = \bar{\epsilon}_{ik} x_k^{j+} + u_i^* \tag{B.2}$$

$$u_i^{j-} = \bar{\epsilon}_{ik} x_k^{j-} + u_i^* \tag{B.3}$$

where u_i^{j+} is the displacement of node n on one surface of the RVE, u_i^{j-} is the displacement of the corresponding node on the opposite side of the RVE (if the RVE is centered in the origin, the index “j+” means along the positive direction of X_j axis, whereas “j-” means along the negative direction of X_j axis), $\bar{\epsilon}_{ik}$ is the average strain of the RVE, x_k is the x coordinate of node k within the RVE, u_i^* is the periodic part of the displacement components on the boundary surfaces and is dependent on the global loads applied.

The difference between Eqs. (B.2) and (B.3) is

$$u_i^{j+} - u_i^{j-} = \bar{\epsilon}_{ik}(x_k^{j+} - x_k^{j-}) = \bar{\epsilon}_{ik} \Delta x_k \tag{B.4}$$

where Δx_k^j represents the dimensions of the RVE along direction k .

For a parallel RVE model, such as the cubic unit cell, Δx_k is constant for each pair of the nodes located on the parallel boundary surfaces, edges and corner vertices. Therefore, Eq. (B.4) can be easily implemented in the finite element analysis as a nodal displacement constraint and the following BCs are obtained:

$$u_i^{j+}(x, y, z) - u_i^{j-}(x, y, z) = c_i^j \quad i, j = 1, 2, 3 \tag{B.5}$$

where c_1^1, c_2^2, c_3^3 represent the average stretch or contraction of the RVE due to the action of the three normal traction component, while $c_2^1 = c_1^2, c_3^1 = c_1^3, c_3^2 = c_2^3$ correspond to the shear deformations due to the three shear traction components.

It can be seen from Eq. (B.5) that, although the difference of the displacements for the corresponding points on the two opposite boundary surfaces is specified, the individual displacement component is still a function of the coordinates, i.e. a plane does not necessarily remain a plane after the deformation.

When Eq. (B.5) is applied, the continuity of the displacement field is guaranteed, while the traction continuity can be imposed through:

$$t_i^+ = -t_i^- \quad \text{with} \quad t_i = \bar{\sigma}_{ik} n_k \tag{B.6}$$

therefore the PBCs on the boundary δV of a RVE can be summarized as follows:

$$u_i^+ - u_i^- = \epsilon_{ik}(x_k^+ - x_k^-) = \Delta u_i \quad \text{and} \quad t_i^+ = t_i^- \tag{B.7}$$

The application of the former of Eq. (B.7) guarantees the uniqueness of the solution, making unnecessary the latter to be explicitly applied in the analysis [33,76]. It has to be pointed out, that, since the displacement BCs are not prescribed for any point, the translational rigid body motions of the RVE are allowed. Moreover, special care has to be taken to avoid over constraints on the edges and corner nodes of the RVE.

As it is performed in the homogenization algorithm with UBCs, six different simulations are required to compute all the entries of the homogenized elasticity tensor. For each of those, a loading condition consisting in a uniform strain with all null components except one is applied to the RVE. Once the numerical computation has been carried out, the components of the elasticity tensor can be retrieved using one of the methods presented in Appendix A.2.

Many numerical studies showed that periodic BCs represent the most efficient choice of BCs in terms of the convergence of the effective material properties with respect to the RVE size. They can be exploited even in case of non-periodic arrangements of the micro-structure. Therefore, periodic BCs are widely used to estimate the effective properties of heterogeneous materials.

In the context of FE method, two types of meshes can be used for PBCs [59]:

- **Periodic mesh:** it is characterized by the same distribution of the nodes on opposite boundaries of the RVE (i.e. the positive and negative parts). In case of a periodic mesh the imposition of PBCs becomes trivial, since opposite nodes can be easily coupled together. Examples of the implementation of the homogenization procedure with PBCs can be found in [37,34,36,35,33,38];
- **Non-periodic mesh:** in more general cases, the same distribution of nodes on opposite parts of the RVE boundary does not hold. Therefore, for a node on a boundary there is not always a conforming node on the opposite side. In this case, a suitable method based on interpolation should be implemented to effectively couple boundary nodes. Different procedures to implement the homogenization algorithm with interpolation-based PBCs on arbitrary mesh are reported in [59,77–79,36].

B.2.1. PBCs on periodic mesh and relative coupling

As previously pointed out, periodic meshes have the same configuration of nodes and element faces on each periodic surface pair of the RVE boundaries. In this case the application of PBCs is easier, because each node on a surface has got exactly only one pairing node on the opposite boundary face. PBCs can be applied in FEA through linear multi-point constraints (MPCs), that are defined as a linear combination of nodal displacements equal to zero [35,34]:

$$\eta_1 u_i^P + \eta_2 u_i^Q + \dots + \eta_n u_i^N = 0 \tag{B.8}$$

where u_i^P is the nodal displacement at the DoF i of the node P and η_n are the coefficients that define the relative motion of the nodes.

The displacement constraint in Eq. (B.7) is introduced into the system of linear MPC equations through a Reference Point (RP), that does not correspond to a physical part of the RVE, but provides the necessary DoF to control its mechanical response. The general form of the equation used to set MPCs is

$$u_i^{k+} - u_i^{k-} = u_i^{RP} \tag{B.9}$$

where $k+$ and $k-$ represent the node sets of two opposite faces and u_i^{RP} is the displacements perturbation carried by the RP.

This constraint equation is applied to all the nodes located on the parallel boundary surfaces of the RVE. It should be noticed that if a DoF of a node is used in a constraint equation, it cannot be involved in another MPC, because that DoF has been eliminated by the existing constraint equation. Thus, particular attention should be used in the formulation of MPC equation of nodes on the edges and vertices of the RVE to avoid over-constraint.

The first step for the application of MPCs consists in the classification into sets of the nodes located on the boundaries of the RVE. There are three main categories of node sets:

- **Inner face:** nodes on a boundary face of the RVE that are not located either on the edges or corners;
- **Inner edge:** nodes on an edge of the RVE, excluding the end nodes on corners;
- **Corner:** a vertex of the RVE.

Table B.8 summarizes and classifies all the node sets required for the implementation of the MPC equations.

Table B.8
Node sets required for MPCs.

Inner faces	$X_m^-, X_p^+,$ $Y_m^-, Y_p^+,$ Z_m^-, Z_p^+
Inner edges	$X_m^- Y_m^-, X_m^- Y_p^+, X_m^- Z_m^-, X_m^- Z_p^+,$ $X_p^+ Y_m^-, X_p^+ Y_p^+, X_p^+ Z_m^-, X_p^+ Z_p^+,$ $Y_m^- Z_m^-, Y_m^- Z_p^+, Y_p^+ Z_m^-, Y_p^+ Z_p^+$
Corners	$X_m^- Y_m^- Z_m^-, X_m^- Y_m^- Z_p^+,$ $X_m^- Y_p^+ Z_m^-, X_m^- Y_p^+ Z_p^+,$ $X_p^+ Y_m^- Z_m^-, X_p^+ Y_m^- Z_p^+,$ $X_p^+ Y_p^+ Z_m^-, X_p^+ Y_p^+ Z_p^+$

Table B.9
MPC equations implementation for all the involved node sets.

MPC with relative coupling	
Inner Face	$u^{Xp} - u^{Xm} = u^{RP1}$ $u^{Yp} - u^{Ym} = u^{RP2}$ $u^{Zp} - u^{Zm} = u^{RP3}$
Inner Edge	$u^{XpZp} - u^{XmZp} = u^{RP1}$ $u^{XpZm} - u^{XmZm} = u^{RP1}$ $u^{XpYm} - u^{XmYm} = u^{RP1}$ $u^{XmYp} - u^{XmYm} = u^{RP2}$ $u^{YpZm} - u^{YmZm} = u^{RP2}$ $u^{XpYp} - u^{XpYm} = u^{RP2}$ $u^{XmZp} - u^{XmZm} = u^{RP3}$ $u^{YpZp} - u^{YpZm} = u^{RP3}$ $u^{YmZp} - u^{YmZm} = u^{RP3}$
Corner	$u^{XpYpZp} - u^{XmYpZp} = u^{RP1}$ $u^{XpYpZm} - u^{XmYpZm} = u^{RP1}$ $u^{XpYmZp} - u^{XmYmZp} = u^{RP1}$ $u^{XpYmZm} - u^{XmYmZm} = u^{RP1}$ $u^{XmYpZm} - u^{XmYmZm} = u^{RP2}$ $u^{XmYpZp} - u^{XmYpZm} = u^{RP3}$ $u^{XmYmZp} - u^{XmYmZm} = u^{RP3}$

In Table B.8 the subscript m and p stand for minus and plus, respectively, and they are referred to negative and positive boundary faces.

The above mentioned node sets can be used to facilitate the coupling of opposite nodes and the linking of nodal degrees of freedom to implement PBCs. As it has already been explained in Appendix B.2, the determination of the effective elastic properties for lattice structures implies a homogenization procedure that requires the application of six independent loading conditions on the RVE. They are summarized as follows:

$$\begin{aligned} \epsilon_{ii} = \bar{\epsilon}_{ii} \quad \text{and} \quad \epsilon_{jk} = 0 \quad \text{for tensile deformation,} \\ \epsilon_{ii} = 0 \quad \text{and} \quad \epsilon_{jk} = \bar{\epsilon}_{jk} \quad \text{for shear deformation} \end{aligned} \tag{B.10}$$

As it can be seen from Eq. (B.10), each loading case consists of the specifying displacement fields, that render null all but one of the six independent components of the strain tensor. The detailed implementation of the MPC equations for each node set is presented in Table B.9, while the six loading cases, necessary to compute all the entries of the homogenized elasticity tensor, are presented in Table B.10. u^{RP1} , u^{RP2} and u^{RP3} are displacement vectors of the RPs (RP1, RP2 and RP3), that are introduced into the model to impose the nodal displacement difference related to the macroscopic tension and shear strain $\bar{\epsilon}_{1i}$ ($i = 1, 2, 3$) in direction X_1 , $\bar{\epsilon}_{2i}$ ($i = 1, 2, 3$) in direction X_2 and $\bar{\epsilon}_{3i}$ ($i = 1, 2, 3$) in direction X_3 , respectively, making each MPC equation easy to be implemented.

In this version of the homogenization algorithm with PBC the coupling of node is done through relative coupling, which is the opposite to absolute coupling that will be explained in the next section. This distinction only takes places in the coupling of edges and vertices [80].

Table B.10
Load cases for the PBCs with MPCs.

Homogenization Loading Cases	
Case 1 (tensile loading along x)	$\mathbf{u}^{RP1} = (L_x \bar{\epsilon}_{11}, 0, 0)$ $\mathbf{u}^{RP2} = (0, 0, 0)$ $\mathbf{u}^{RP3} = (0, 0, 0)$
Case 2 (tensile loading along y)	$\mathbf{u}^{RP1} = (0, 0, 0)$ $\mathbf{u}^{RP2} = (0, L_y \bar{\epsilon}_{22}, 0)$ $\mathbf{u}^{RP3} = (0, 0, 0)$
Case 3 (tensile loading along z)	$\mathbf{u}^{RP1} = (0, 0, 0)$ $\mathbf{u}^{RP2} = (0, 0, 0)$ $\mathbf{u}^{RP3} = (0, 0, L_z \bar{\epsilon}_{33})$
Case 4 (shear loading along xy and yx)	$\mathbf{u}^{RP1} = (0, L_y \bar{\epsilon}_{12}/2, 0)$ $\mathbf{u}^{RP2} = (L_x \bar{\epsilon}_{21}/2, 0, 0)$ $\mathbf{u}^{RP3} = (0, 0, 0)$
Case 5 (shear loading along yz and zy)	$\mathbf{u}^{RP1} = (0, 0, 0)$ $\mathbf{u}^{RP2} = (0, 0, L_z \bar{\epsilon}_{23}/2)$ $\mathbf{u}^{RP3} = (0, L_y \bar{\epsilon}_{32}/2, 0)$
Case 6 (shear loading along zx and xz)	$\mathbf{u}^{RP1} = (0, 0, L_z \bar{\epsilon}_{13}/2)$ $\mathbf{u}^{RP2} = (0, 0, 0)$ $\mathbf{u}^{RP3} = (L_x \bar{\epsilon}_{31}/2, 0, 0)$

Taking for example the equations that link the vertices of the negative face along x :

$$\begin{aligned}
 &\mathbf{u}^{XpYmZm} - \mathbf{u}^{XmYmZm} = \mathbf{u}^{RP1} \\
 &\mathbf{u}^{XmYpZm} - \mathbf{u}^{XmYmZm} = \mathbf{u}^{RP2} \\
 &\mathbf{u}^{XpYpZm} - \mathbf{u}^{XmYpZm} = \mathbf{u}^{RP1} \quad \text{or} \quad \mathbf{u}^{XpYpZm} - \mathbf{u}^{XpYmZm} = \mathbf{u}^{RP2},
 \end{aligned} \tag{B.11}$$

only one of the last two equations is needed. It can be noticed that the displacement of the node $XpYpZm$ is linked to that of the nodes $XpYmZm$ and $XmYpZm$. The same holds for node $XmYmZm$. Thus, the set of Eq. (B.11) give the relative formulation of the PBCs.

Once each simulation is completed nodal reaction forces on faces Xp , Yp and Zp , including nodes on edges and corners, are retrieved. Then stresses and coefficients of the elastic tensor are computed following the same procedure presented in Appendix B.1.

B.2.2. PBCs on periodic mesh and absolute coupling

In this section a variation on the most commonly used homogenization algorithm with PBC on a periodic mesh presented in Coluccia and De Pasquale [60,55]. It is based on the original formulation of PBC from Barbero [27], developed for the homogenization of composites. Again, six static simulations are necessary to compute all the components of the stiffness matrix $[E]$, each with the imposition of only one of the six unitary average strain vector $\{\bar{\epsilon}\}$:

$$\bar{\epsilon}_i = \frac{1}{V} \int_V \epsilon_i dV = \epsilon_i^0 \tag{B.12}$$

$$\begin{aligned}
 C_{\alpha\beta} = \bar{\sigma}_\alpha &= \int_V \sigma_\alpha(x_1, x_2, x_3) dV \quad \text{where} \quad \epsilon_\beta^0 = 1 \\
 &\text{for} \quad \alpha, \beta = 1, \dots, 6
 \end{aligned} \tag{B.13}$$

In each simulation a set of PBC linking nodes on opposite sides of the RVE and specific displacement boundary conditions have to be imposed to achieve an overall unitary strain. While applied displacement boundary conditions for each case are the same as those presented in Table B.10, the formulation of PBCs for boundary face, edges and vertices are summarized in Table B.11. The presented algorithm relies on the absolute formulation of PBCs. One vertex and three edges of the unit cell are selected as the local coordinate system and the displacements of the nodes on the other edges and vertices are linked to those located on this local coordinate system. In synthesis, the resulting MPC equations are a

Table B.11
MPC equations implementation for all the involved node sets.

MPC with absolute coupling	
Inner Face	$\mathbf{u}^{Xp} - \mathbf{u}^{Xm} = \mathbf{u}^{RP1}$ $\mathbf{u}^{Yp} - \mathbf{u}^{Ym} = \mathbf{u}^{RP2}$ $\mathbf{u}^{Zp} - \mathbf{u}^{Zm} = \mathbf{u}^{RP3}$
Inner Edge	$\mathbf{u}^{XpYp} - \mathbf{u}^{XmYm} = \mathbf{u}^{RP1} + \mathbf{u}^{RP2}$ $\mathbf{u}^{XpYm} - \mathbf{u}^{XmYp} = \mathbf{u}^{RP1} - \mathbf{u}^{RP2}$ $\mathbf{u}^{XpZp} - \mathbf{u}^{XmZm} = \mathbf{u}^{RP1} + \mathbf{u}^{RP3}$ $\mathbf{u}^{XpZm} - \mathbf{u}^{XmZp} = \mathbf{u}^{RP1} - \mathbf{u}^{RP3}$ $\mathbf{u}^{YpZp} - \mathbf{u}^{YmZm} = \mathbf{u}^{RP2} + \mathbf{u}^{RP3}$ $\mathbf{u}^{YpZm} - \mathbf{u}^{YmZp} = \mathbf{u}^{RP2} - \mathbf{u}^{RP3}$
Corner	$\mathbf{u}^{XpYpZp} - \mathbf{u}^{XmYmZm} = \mathbf{u}^{RP1} + \mathbf{u}^{RP2} + \mathbf{u}^{RP3}$ $\mathbf{u}^{XpYpZm} - \mathbf{u}^{XmYmZp} = \mathbf{u}^{RP1} + \mathbf{u}^{RP2} - \mathbf{u}^{RP3}$ $\mathbf{u}^{XmYpZp} - \mathbf{u}^{XpYmZm} = -\mathbf{u}^{RP1} + \mathbf{u}^{RP2} + \mathbf{u}^{RP3}$ $\mathbf{u}^{XpYmZp} - \mathbf{u}^{XmYpZm} = \mathbf{u}^{RP1} - \mathbf{u}^{RP2} + \mathbf{u}^{RP3}$

linear combination of those used in the relative formulation. Therefore, two macro-strains and dimensions are needed for the coupling of edges and three for vertices.

B.2.3. PBCs on a generic mesh

Generally, the conformity of mesh nodes cannot be always guaranteed, leading to a non-periodic mesh. This is usually the outcome of a more flexible and cheaper meshing algorithm. Thus, it is necessary to find an alternative method to couple nodes on opposite boundary faces and write MPC equations. In literature, several ways to couple nodes on opposite surfaces can be found:

- Nguyen et al. [59] introduced a method based on Lagrange interpolation using the Lagrange shape functions and the cubic spline interpolation using the Hermite shape;
- Ouchetto et al. [78,79] proposed a method that couples a node on a face to the corresponding triangle of the mesh on the opposite face. Then it introduces the MPC equation linking the matching nodes through coefficients, computed using geometric shape functions;
- Wippler et al. [81] implemented the PBCs in an approximate setting using a projection algorithm;
- Reis et al. [77] proposed a Mortar Decomposition Method to enforce PBCs on complex micro-structures with non-conformal meshes.

In this work, the procedure presented by Tian et al. [35,36], that consists in an interpolation algorithm based on geometric shape functions of the element of the non-conformal mesh, is presented. The formulation of the PBCs imposed on the RVE with non-conformal meshes is given through the following modified displacement-difference constraint:

$$\mathbf{u}^{k+} - \mathbf{u}^d = \mathbf{u}^{k+} - \sum_{i=1}^N A_i \mathbf{u}^i = \Delta \bar{\mathbf{u}} \quad \text{on} \quad \delta V \tag{B.14}$$

where \mathbf{u}^d is the interpolated displacement vector of the dummy node, which is the projection on δV^- of the node located on δV^+ , and \mathbf{u}^i is the displacement of the nodes of the element containing the dummy node. The number of interpolation nodes N depends on the type of mesh element: $N = 3$ for the 4-node linear tetrahedral element and $N = 6$ for the 10-node quadratic tetrahedron. The shape functions A_i of the plane triangular face of an element have the expressions summarized in Table B.12, where S_1, S_2, S_3 and S are the areas of the triangles $d-2-3, d-1-3, d-1-2$ and $1-2-3$, respectively, and $S = S_1 + S_2 + S_3$ (see Fig. B.16).

In case of non-conformal meshes the nodal displacement-difference constraint of the PBCs is implemented as follows:

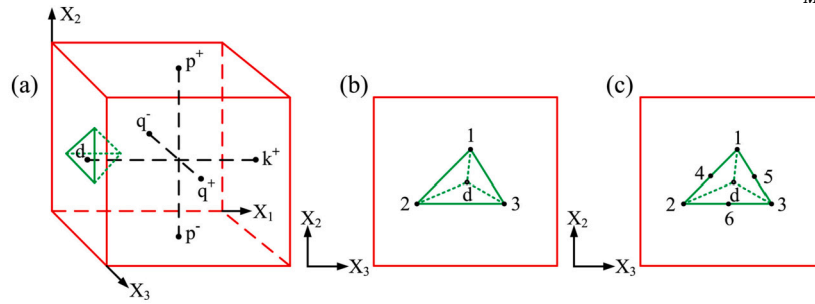


Fig. B.16. (a) A tetrahedron element, (b) the linear tetrahedron element's nodes and (c) the quadratic tetrahedron element's nodes located on the boundaries of the RVE [36].

Table B.12
Shape functions for linear and quadratic tetrahedral elements.

Shape functions	
Linear tetrahedron	$A_1 = \frac{S_1}{S}$ $A_2 = \frac{S_2}{S}$ $A_3 = \frac{S_3}{S}$
Quadratic tetrahedron	$A_1 = \left(\frac{2S_1}{S} - 1\right) \frac{S_1}{S}$ $A_2 = \left(\frac{2S_2}{S} - 1\right) \frac{S_2}{S}$ $A_3 = \left(\frac{2S_3}{S} - 1\right) \frac{S_3}{S}$ $A_4 = \frac{4S_1}{S} \frac{S_2}{S}$ $A_5 = \frac{4S_1}{S} \frac{S_3}{S}$ $A_6 = \frac{4S_2}{S} \frac{S_3}{S}$

Table B.13
Definition of XpS , YpS and ZpS node sets.

Node sets for the implementation of PBCs	
XpS	Xp , $XpYm$, $XpZm$, $XpZp$, $XpYmZm$, $XpYmZp$, $XpYpZm$, $XpYpZp$
YpS	Yp , $XmYp$, $XmZm$, $YpZm$, $XmYpZm$
ZpS	Zp , $XmZp$, $YmZp$, $YpZp$, $XmYmZp$, $XmYpZp$

$$\begin{aligned}
 \mathbf{u}^{XpS} - \sum_{i=1}^N A_i \mathbf{u}^{XmS} &= \mathbf{u}^{RP1} \\
 \mathbf{u}^{YpS} - \sum_{i=1}^N A_i \mathbf{u}^{YmS} &= \mathbf{u}^{RP2} \\
 \mathbf{u}^{ZpS} - \sum_{i=1}^N A_i \mathbf{u}^{ZmS} &= \mathbf{u}^{RP3}
 \end{aligned} \tag{B.15}$$

where XpS , YpS and ZpS node sets are obtained from the ones presented in Table B.8 and their definition can be found in Table B.13. XmS , YmS and ZmS are the node sets composed of all the nodes on the surfaces with the minimum x , y and z coordinate, respectively.

Once the MPC equation has been set, the homogenization algorithm follows the same path as that used with periodic conformal meshes: six loading cases are simulated using the BCs presented in Table B.10. After each simulation, reaction forces are retrieved and the coefficient of the elastic tensor is computed, as presented in Appendix B.1.

Table B.14
Strategies for calculation of homogenized properties with the energy method.

Expressions for effective properties	Boundary conditions
$\bar{C}_{11} = U / (0.5 \bar{\epsilon}_{11}^2 V_{RVE})$	$\bar{\epsilon}_{11} \neq 0, \bar{\epsilon}_{22} = \bar{\epsilon}_{33} = \bar{\epsilon}_{23} = \bar{\epsilon}_{13} = \bar{\epsilon}_{12} = 0$
$\bar{C}_{22} = U / (0.5 \bar{\epsilon}_{22}^2 V_{RVE})$	$\bar{\epsilon}_{22} \neq 0, \bar{\epsilon}_{11} = \bar{\epsilon}_{33} = \bar{\epsilon}_{23} = \bar{\epsilon}_{13} = \bar{\epsilon}_{12} = 0$
$\bar{C}_{33} = U / (0.5 \bar{\epsilon}_{33}^2 V_{RVE})$	$\bar{\epsilon}_{33} \neq 0, \bar{\epsilon}_{11} = \bar{\epsilon}_{22} = \bar{\epsilon}_{23} = \bar{\epsilon}_{13} = \bar{\epsilon}_{12} = 0$
$\bar{C}_{44} = U / (0.5 \bar{\epsilon}_{23}^2 V_{RVE})$	$\bar{\epsilon}_{23} \neq 0, \bar{\epsilon}_{11} = \bar{\epsilon}_{22} = \bar{\epsilon}_{33} = \bar{\epsilon}_{13} = \bar{\epsilon}_{12} = 0$
$\bar{C}_{55} = U / (0.5 \bar{\epsilon}_{13}^2 V_{RVE})$	$\bar{\epsilon}_{13} \neq 0, \bar{\epsilon}_{11} = \bar{\epsilon}_{22} = \bar{\epsilon}_{33} = \bar{\epsilon}_{23} = \bar{\epsilon}_{12} = 0$
$\bar{C}_{66} = U / (0.5 \bar{\epsilon}_{12}^2 V_{RVE})$	$\bar{\epsilon}_{12} \neq 0, \bar{\epsilon}_{11} = \bar{\epsilon}_{22} = \bar{\epsilon}_{33} = \bar{\epsilon}_{23} = \bar{\epsilon}_{13} = 0$
$\bar{C}_{12} = \bar{C}_{21} = U^{12} / \bar{\epsilon}_{11} \bar{\epsilon}_{22}$	$\bar{\epsilon}_{11} \neq 0, \bar{\epsilon}_{22} \neq 0,$
$U^{12} = U / V_{RVE} - (0.5 \bar{C}_{11} \bar{\epsilon}_{11}^2) - (0.5 \bar{C}_{22} \bar{\epsilon}_{22}^2),$	$\bar{\epsilon}_{33} = \bar{\epsilon}_{23} = \bar{\epsilon}_{13} = \bar{\epsilon}_{12} = 0,$
$\bar{C}_{23} = \bar{C}_{32} = U^{23} / \bar{\epsilon}_{22} \bar{\epsilon}_{33}$	$\bar{\epsilon}_{22} \neq 0, \bar{\epsilon}_{33} \neq 0,$
$U^{23} = U / V_{RVE} - (0.5 \bar{C}_{22} \bar{\epsilon}_{22}^2) - (0.5 \bar{C}_{33} \bar{\epsilon}_{33}^2),$	$\bar{\epsilon}_{23} = \bar{\epsilon}_{13} = \bar{\epsilon}_{12} = \bar{\epsilon}_{11} = 0,$
$\bar{C}_{13} = \bar{C}_{31} = U^{13} / \bar{\epsilon}_{11} \bar{\epsilon}_{33}$	$\bar{\epsilon}_{11} \neq 0, \bar{\epsilon}_{33} \neq 0,$
$U^{13} = U / V_{RVE} - (0.5 \bar{C}_{11} \bar{\epsilon}_{11}^2) - (0.5 \bar{C}_{33} \bar{\epsilon}_{33}^2),$	$\bar{\epsilon}_{22} = \bar{\epsilon}_{23} = \bar{\epsilon}_{13} = \bar{\epsilon}_{12} = 0,$

B.3. Numerical implementation of the energy method

The homogenization algorithms, which have been previously presented, are specifically designed for the computation of the entries of the homogenized elasticity tensor through nodal reaction forces or stress values. However, for the application of the energy method, presented in Appendix A.2, three additional load cases are required for the computation of the off-diagonal entries. The complete set of BCs for each loading case and the equations to retrieve the entries of the elasticity tensor are reported in Table B.14 [82]. The coupling of the nodes on opposite faces of the RVE is performed in the same way as presented in Appendix B.2.1, as well as the imposition of BCs through RPs.

After the FEA of each loading cases the microscale energies are retrieved and the total deformation energy can be computed through one of the relations in Eq. (A.19). Finally the entries \bar{C}_{ij} of the homogenized elasticity tensor can be computed through the equations in Table B.14 for the corresponding loading case.

Data availability

Data will be made available on request.

References

- [1] A.G. Evans, J.W. Hutchinson, N.A. Fleck, M.F. Ashby, H.N.G. Wadley, The topological design of multifunctional cellular metals, Prog. Mater. Sci. 46 (3) (2001) 309–327, [https://doi.org/10.1016/S0079-6425\(00\)00016-5](https://doi.org/10.1016/S0079-6425(00)00016-5), <https://www.sciencedirect.com/science/article/pii/S0079642500000165>.
- [2] H.N. Wadley, Multifunctional periodic cellular metals, Philos. Trans. - Royal Soc., Math. Phys. Eng. Sci. 364 (1838) (2005) 31–68, <https://doi.org/10.1098/rsta.2005.1697>, <https://royalsocietypublishing.org/doi/10.1098/rsta.2005.1697>.
- [3] C. Yan, L. Hao, A. Hussein, S.L. Bubb, P. Young, D. Raymont, Evaluation of light-weight AlSi10Mg periodic cellular lattice structures fabricated via direct metal laser sintering, J. Mater. Process. Technol. 214 (4)

- (2014) 856–864, <https://doi.org/10.1016/j.jmatprotec.2013.12.004>, <https://www.sciencedirect.com/science/article/pii/S0924013613003804>.
- [4] J. Plocher, A. Panesar, Review on design and structural optimisation in additive manufacturing: towards next-generation lightweight structures, *Mater. Des.* 183 (2019) 108164, <https://doi.org/10.1016/j.matdes.2019.108164>, <https://www.sciencedirect.com/science/article/pii/S0264127519306021>.
- [5] J. Zhu, H. Zhou, C. Wang, L. Zhou, S. Yuan, W. Zhang, A review of topology optimization for additive manufacturing: status and challenges, *Chin. J. Aeronaut.* 34 (1) (2021) 91–110, <https://doi.org/10.1016/j.cja.2020.09.020>, <https://www.sciencedirect.com/science/article/pii/S1000936120304520>.
- [6] L.K. Dharmalingam, V. Aute, J. Ling, Review of triply periodic minimal surface (TPMS) based heat exchanger designs, in: *Proceeding of International Heat Transfer Conference*, vol. 17, 2022, p. 10.
- [7] K. Dutkowsk, M. Kruzal, K. Rokosz, Review of the state-of-the-art uses of minimal surfaces in heat transfer, *Energies* 15 (21) (2022), <https://doi.org/10.3390/en15217994>.
- [8] A. Fawaz, Y. Hua, S. Le Corre, Y. Fan, L. Luo, Topology optimization of heat exchangers: a review, *Energy* 252 (2022) 124053, <https://doi.org/10.1016/j.energy.2022.124053>, <https://www.sciencedirect.com/science/article/pii/S0360544222009562>.
- [9] I. Kaur, P. Singh, State-of-the-art in heat exchanger additive manufacturing, *Int. J. Heat Mass Transf.* 178 (2021) 121600, <https://doi.org/10.1016/j.ijheatmasstransfer.2021.121600>, <https://www.sciencedirect.com/science/article/pii/S0017931021007031>.
- [10] Y. Wang, X. Ren, Z. Chen, Y. Jiang, X. Cao, S. Fang, T. Zhao, Y. Li, D. Fang, Numerical and experimental studies on compressive behavior of Gyroid lattice cylindrical shells, *Mater. Des.* 186 (2020) 108340, <https://doi.org/10.1016/j.matdes.2019.108340>, <https://www.sciencedirect.com/science/article/pii/S0264127519307786>.
- [11] M. Benedetti, A. du Plessis, R. Ritchie, M. Dallago, N. Razavi, F. Berto, Architected cellular materials: a review on their mechanical properties towards fatigue-tolerant design and fabrication, *Mater. Sci. Eng., R Rep.* 144 (2021) 100606, <https://doi.org/10.1016/j.mser.2021.100606>, <https://www.sciencedirect.com/science/article/pii/S0927796X21000012>.
- [12] Z. Ozdemir, E. Hernandez-Nava, A. Tyas, J.A. Warren, S.D. Fay, R. Goodall, I. Todd, H. Askes, Energy absorption in lattice structures in dynamics: experiments, *Int. J. Impact Eng.* 89 (2016) 49–61, <https://doi.org/10.1016/j.ijimpeng.2015.10.007>, <https://www.sciencedirect.com/science/article/pii/S0734743X15002134>.
- [13] H. Yin, W. Zhang, L. Zhu, F. Meng, J. Liu, G. Wen, Review on lattice structures for energy absorption properties, *Compos. Struct.* 304 (2023) 116397, <https://doi.org/10.1016/j.compstruct.2022.116397>, <https://www.sciencedirect.com/science/article/pii/S0263822322011291>.
- [14] S. Li, H. Zhu, G. Feng, L. Xiao, W. Song, Influence mechanism of cell-arrangement strategy on energy absorption of dual-phase hybrid lattice structure, *Int. J. Impact Eng.* 175 (2023) 104528, <https://doi.org/10.1016/j.ijimpeng.2023.104528>, <https://www.sciencedirect.com/science/article/pii/S0734743X23000398>.
- [15] L. Xiao, G. Shi, G. Feng, S. Li, S. Liu, W. Song, Large deformation response of a novel triply periodic minimal surface skeletal-based lattice metamaterial with high stiffness and energy absorption, *Int. J. Solids Struct.* 296 (2024) 112830, <https://doi.org/10.1016/j.ijsolstr.2024.112830>, <https://www.sciencedirect.com/science/article/pii/S0020768324001896>.
- [16] G. Comandini, M. Ouisse, V.P. Ting, F. Scarpa, Acoustic transmission loss in Hilbert fractal metamaterials, *Sci. Rep.* 13 (1) (2023) 19058, <https://doi.org/10.1038/s41598-023-43646-1>, <https://www.nature.com/articles/s41598-023-43646-1>.
- [17] G. Comandini, C. Khodr, V.P. Ting, M. Azarpeyvand, F. Scarpa, Sound absorption in Hilbert fractal and coiled acoustic metamaterials, *Appl. Phys. Lett.* 120 (6) (2022) 061902, <https://doi.org/10.1063/5.0079531>.
- [18] S.A. Naghavi, M. Tamaddon, A. Marghoub, K. Wang, B.B. Babamiri, K. Hazeli, W. Xu, X. Lu, C. Sun, L. Wang, M. Moazen, L. Wang, D. Li, C. Liu, Mechanical characterisation and numerical modelling of TPMS-based gyroid and diamond Ti6Al4V scaffolds for bone implants: an integrated approach for translational consideration, *Bioengineering* 9 (10) (2022) 504, <https://doi.org/10.3390/bioengineering9100504>, <https://www.mdpi.com/2306-5354/9/10/504>.
- [19] S. Ma, Q. Tang, Q. Feng, J. Song, X. Han, F. Guo, Mechanical behaviours and mass transport properties of bone-mimicking scaffolds consisted of gyroid structures manufactured using selective laser melting, *J. Mech. Behav. Biomed. Mater.* 93 (2019) 158–169, <https://doi.org/10.1016/j.jmbbm.2019.01.023>, <https://www.sciencedirect.com/science/article/pii/S175161611831258X>.
- [20] N. Wang, G.K. Meenashisundaram, S. Chang, J.Y.H. Fuh, S.T. Dheen, A. Senthil Kumar, A comparative investigation on the mechanical properties and cytotoxicity of Cubic, Octet, and TPMS gyroid structures fabricated by selective laser melting of stainless steel 316L, *J. Mech. Behav. Biomed. Mater.* 129 (2022) 105151, <https://doi.org/10.1016/j.jmbbm.2022.105151>, <https://www.sciencedirect.com/science/article/pii/S1751616122000741>.
- [21] A. Wiberg, J. Persson, J. Ölvander, Design for additive manufacturing – a review of available design methods and software, *Rapid Prototyping J.* 25 (6) (2019) 1080–1094, <https://doi.org/10.1108/RPJ-10-2018-0262>, <https://www.emerald.com/insight/content/doi/10.1108/RPJ-10-2018-0262/full/html>.
- [22] M. Helou, S. Kara, Design, analysis and manufacturing of lattice structures: an overview, *Int. J. Comput. Integr. Manuf.* 31 (3) (2018) 243–261, <https://doi.org/10.1080/0951192X.2017.1407456>.
- [23] P. Terriault, V. Brailovsk, Modeling and simulation of large, conformal, porosity-graded and lightweight lattice structures made by additive manufacturing, *Finite Elem. Anal. Des.* 138 (2018) 1–11, <https://doi.org/10.1016/j.finel.2017.09.005>, <https://www.sciencedirect.com/science/article/pii/S0168874X16305923>.
- [24] A. Srivastava, Elastic metamaterials and dynamic homogenization: a review, *Int. J. Smart Nano Mater.* 6 (1) (2015) 41–60, <https://doi.org/10.1080/19475411.2015.1017779>.
- [25] B. Hassani, E. Hinton, A review of homogenization and topology optimization I—homogenization theory for media with periodic structure, *Comput. Struct.* 69 (6) (1998) 707–717, [https://doi.org/10.1016/S0045-7949\(98\)00131-X](https://doi.org/10.1016/S0045-7949(98)00131-X), <https://www.sciencedirect.com/science/article/pii/S004579499800131X>.
- [26] C.K. Yan, On Homogenization and De-homogenization of Composite Materials, Doctor of Philosophy, Drexel University, Nov. 2003, <https://doi.org/10.17918/etd-246>, <https://ResearchDiscovery.drexel.edu/esplorero/outputs/doctoral/991014632333804721>.
- [27] E.J. Barbero, *Finite Element Analysis of Composite Materials Using Abaqus™*, Composite Materials: Design and Analysis, CRC Press, Taylor & Francis Group, Boca Raton London New York, 2013.
- [28] J. Somnic, B.W. Jo, Status and challenges in homogenization methods for lattice materials, *Materials* 15 (2) (2022) 605, <https://doi.org/10.3390/ma15020605>, <https://www.mdpi.com/1996-1944/15/2/605>.
- [29] W. Yu, An introduction to micromechanics, *Appl. Mech. Mater.* 828 (2016) 3–24, <https://doi.org/10.4028/www.scientific.net/AMM.828.3>, <https://www.scientific.net/AMM.828.3>.
- [30] F.J.V. Ribeiro, S.L.M.R. Filho, M.E. Silveira, T.H. Panzera, F. Scarpa, M.L.P. Tonatto, A sequential multiscale technique to evaluate the mechanical behaviour of hybrid composites containing carbon fibre and silica microparticles, *Compos. Struct.* 314 (2023) 116977, <https://doi.org/10.1016/j.compstruct.2023.116977>, <https://linkinghub.elsevier.com/retrieve/pii/S0263822323003215>.
- [31] G. Steven, Homogenization and inverse homogenization for 3D composites of complex architecture, *Eng. Comput.* 23 (4) (2006) 432–450, <https://doi.org/10.1108/02644400610661181>, <https://www.emerald.com/insight/content/doi/10.1108/02644400610661181/full/html>.
- [32] G.P. Steven, Homogenization of multicomponent composite orthotropic materials using FEA, *Commun. Numer. Methods Eng.* 13 (7) (1997) 517–531, [https://doi.org/10.1002/\(SICI\)1099-0887\(199707\)13:7<517::AID-CNMM74>3.0.CO;2-L](https://doi.org/10.1002/(SICI)1099-0887(199707)13:7<517::AID-CNMM74>3.0.CO;2-L), [https://onlinelibrary.wiley.com/doi/10.1002/\(SICI\)1099-0887\(199707\)13:7<517::AID-CNMM74>3.0.CO;2-L](https://onlinelibrary.wiley.com/doi/10.1002/(SICI)1099-0887(199707)13:7<517::AID-CNMM74>3.0.CO;2-L).
- [33] Z. Xia, Y. Zhang, F. Ellyin, A unified periodical boundary conditions for representative volume elements of composites and applications, *Int. J. Solids Struct.* 40 (8) (2003) 1907–1921, [https://doi.org/10.1016/S0020-7683\(03\)00024-6](https://doi.org/10.1016/S0020-7683(03)00024-6), <https://www.sciencedirect.com/science/article/pii/S0020768303000246>.
- [34] S.L. Omairey, P.D. Dunning, S. Sriramula, Development of an ABAQUS plugin tool for periodic RVE homogenisation, *Eng. Comput.* 35 (2) (2019) 567–577, <https://doi.org/10.1007/s00366-018-0616-4>.
- [35] W. Tian, L. Qi, X. Chao, J. Liang, M. Fu, Periodic boundary condition and its numerical implementation algorithm for the evaluation of effective mechanical properties of the composites with complicated micro-structures, *Composites, Part B, Eng.* 162 (2019) 1–10, <https://doi.org/10.1016/j.compositesb.2018.10.053>, <https://linkinghub.elsevier.com/retrieve/pii/S1359836818319838>.
- [36] W. Tian, L. Qi, Unified periodic boundary condition for homogenizing the thermo-mechanical properties of composites, *Appl. Math. Model.* 121 (2023) 252–269, <https://doi.org/10.1016/j.apm.2023.04.024>, <https://www.sciencedirect.com/science/article/pii/S0307904X23001762>.
- [37] L. Mizzi, D. Attard, R. Gatt, K.K. Dudek, B. Ellul, J.N. Grima, Implementation of periodic boundary conditions for loading of mechanical metamaterials and other complex geometric microstructures using finite element analysis, *Eng. Comput.* 37 (3) (2021) 1765–1779, <https://doi.org/10.1007/s00366-019-00910-1>.
- [38] C. Ye, C. Zhang, J. Zhao, Y. Dong, Effects of post-processing on the surface finish, porosity, residual stresses, and fatigue performance of additive manufactured metals: a review, *J. Mater. Eng. Perform.* 30 (9) (2021) 6407–6425, <https://doi.org/10.1007/s11665-021-06021-7>.
- [39] C. Wang, L. Feng, I. Jasiuk, Scale and boundary conditions effects on the apparent elastic moduli of trabecular bone modeled as a periodic cellular solid, *J. Biomech. Eng.* 131 (121008) (Nov. 2009), <https://doi.org/10.1115/1.4000192>.
- [40] S. Xu, J. Shen, S. Zhou, X. Huang, Y.M. Xie, Design of lattice structures with controlled anisotropy, *Mater. Des.* 93 (2016) 443–447, <https://doi.org/10.1016/j.matdes.2016.01.007>, <https://www.sciencedirect.com/science/article/pii/S0264127516300120>.
- [41] P. Lohmuller, J. Favre, S. Kenzari, B. Piotrowski, L. Peltier, P. Laheurte, Architectural effect on 3D elastic properties and anisotropy of cubic lattice structures, *Mater. Des.* 182 (2019) 108059, <https://doi.org/10.1016/j.matdes.2019.108059>, <https://www.sciencedirect.com/science/article/pii/S0264127519304976>.
- [42] O. Al-Ketan, R.K. Abu Al-Rub, R. Rowshan, The effect of architecture on the mechanical properties of cellular structures based on the IWP minimal surface, *J. Mater. Res.* 33 (3) (2018) 343–359, <https://doi.org/10.1557/jmr.2018.1>, <http://link.springer.com/10.1557/jmr.2018.1>.
- [43] P. Lohmuller, J. Favre, B. Piotrowski, S. Kenzari, P. Laheurte, Stress concentration and mechanical strength of cubic lattice architectures, *Materials* 11 (7) (2018) 1146, <https://doi.org/10.3390/ma11071146>, <https://www.mdpi.com/1996-1944/11/7/1146>.
- [44] C. Bonatti, D. Mohr, Smooth-shell metamaterials of cubic symmetry: anisotropic elasticity, yield strength and specific energy absorption, *Acta Mater.* 164

- (2019) 301–321, <https://doi.org/10.1016/j.actamat.2018.10.034>, <https://www.sciencedirect.com/science/article/pii/S1359645418308346>.
- [45] C. Chatzigeorgiou, B. Piotrowski, Y. Chemisky, P. Laheurte, F. Meraghni, Numerical investigation of the effective mechanical properties and local stress distributions of TPMS-based and strut-based lattices for biomedical applications, *J. Mech. Behav. Biomed. Mater.* 126 (2022) 105025, <https://doi.org/10.1016/j.jmbbm.2021.105025>, <https://linkinghub.elsevier.com/retrieve/pii/S1751616121006512>.
- [46] A. Pais, J.L. Alves, R.N. Jorge, J. Belinha, Multiscale homogenization techniques for TPMS foam material for biomedical structural applications, *Bioengineering* 10 (5) (2023) 515, <https://doi.org/10.3390/bioengineering10050515>, <https://www.mdpi.com/2306-5354/10/5/515>.
- [47] D. Li, W. Liao, N. Dai, G. Dong, Y. Tang, Y.M. Xie, Optimal design and modeling of gyroid-based functionally graded cellular structures for additive manufacturing, *Comput. Aided Des.* 104 (2018) 87–99, <https://doi.org/10.1016/j.cad.2018.06.003>, <https://linkinghub.elsevier.com/retrieve/pii/S0010448518300381>.
- [48] C. Imediegwu, R. Murphy, R. Hewson, M. Santer, Multiscale structural optimization towards three-dimensional printable structures, *Struct. Multidiscip. Optim.* 60 (2) (2019) 513–525, <https://doi.org/10.1007/s00158-019-02220-y>.
- [49] C. Imediegwu, R. Murphy, R. Hewson, M. Santer, Multiscale thermal and thermostructural optimization of three-dimensional lattice structures, *Struct. Multidiscip. Optim.* 65 (1) (2021) 13, <https://doi.org/10.1007/s00158-021-03087-8>.
- [50] R.R. Fernandes, A.Y. Tamijani, Design optimization of lattice structures with stress constraints, *Mater. Des.* 210 (2021) 110026, <https://doi.org/10.1016/j.matdes.2021.110026>, <https://linkinghub.elsevier.com/retrieve/pii/S0264147251005815>.
- [51] N. Strömberg, A new multi-scale topology optimization framework for optimal combinations of macro-layouts and local gradings of TPMS-based lattice structures, *Mech. Based Des. Struct. Mach.* 52 (1) (2022) 257–274, <https://doi.org/10.1080/15397734.2022.2107538>.
- [52] M. Zhmaylo, L. Maslov, A. Borovkov, F. Tarasenko, Finite element homogenization and experimental evaluation of additively manufactured lattice metamaterials, *J. Braz. Soc. Mech. Sci. Eng.* 45 (6) (2023) 299, <https://doi.org/10.1007/s40430-023-04210-0>.
- [53] D. Montoya-Zapata, D.A. Acosta, C. Cortés, J. Pareja-Corcho, A. Moreno, J. Posada, O. Ruiz-Salguero, Approximation of the mechanical response of large lattice domains using homogenization and design of experiments, *Appl. Sci.* 10 (11) (2020) 3858, <https://doi.org/10.3390/app10113858>, <https://www.mdpi.com/2076-3417/10/11/3858>.
- [54] D. Montoya-Zapata, D.A. Acosta, C. Cortés, J. Pareja-Corcho, A. Moreno, J. Posada, O. Ruiz-Salguero, Meta-modeling of lattice mechanical responses via design of experiments, in: 2020 International Conference on Mathematics and Computers in Science and Engineering (MACISE), 2020, pp. 308–317, <https://ieeexplore.ieee.org/document/9195607>.
- [55] A. Coluccia, G. De Pasquale, Strain-based method for fatigue failure prediction of additively manufactured lattice structures, *Sci. Rep.* 13 (1) (2023) 22775, <https://doi.org/10.1038/s41598-023-49846-z>, <https://www.nature.com/articles/s41598-023-49846-z>.
- [56] P. Tan, L. Tong, G.P. Steven, Behavior of 3D orthogonal woven CFRP composites. Part II. FEA and analytical modeling approaches, *Composites, Part A, Appl. Sci. Manuf.* 31 (3) (2000) 273–281, [https://doi.org/10.1016/S1359-835X\(99\)00071-8](https://doi.org/10.1016/S1359-835X(99)00071-8).
- [57] R. Hill, Elastic properties of reinforced solids: some theoretical principles, *J. Mech. Phys. Solids* 11 (5) (1963) 357–372, [https://doi.org/10.1016/0022-5096\(63\)90036-X](https://doi.org/10.1016/0022-5096(63)90036-X), <https://linkinghub.elsevier.com/retrieve/pii/002250966390036X>.
- [58] D. Garoz Gómez, F.A. Gilabert, R. Sevenois, S. Spronk, A. Rezaei, W. Van Paepegem, Definition of periodic boundary conditions in explicit dynamic simulations of micro- or meso-scale unit cells with conformal and non-conformal meshes, in: 17th European Conference on Composite Materials, Munich, Germany, European Society for Composite Materials (ESCM), ISBN 978-3-00-053387-7, 2016, pp. 1–6.
- [59] V.D. Nguyen, E. Béchet, C. Geuzaine, L. Noels, Imposing periodic boundary condition on arbitrary meshes by polynomial interpolation, *Comput. Mater. Sci.* 55 (2012) 390–406, <https://doi.org/10.1016/j.commatsci.2011.10.017>, <https://www.sciencedirect.com/science/article/pii/S0927025611005866>.
- [60] G. De Pasquale, M. Montemurro, A. Catapano, G. Bertolino, L. Revelli, Cellular structures from additive processes: design, homogenization and experimental validation, *Proc. Struct. Integr.* 8 (2018) 75–82, <https://doi.org/10.1016/j.prostr.2017.12.009>, <https://www.sciencedirect.com/science/article/pii/S2452321617305024>.
- [61] M. Moeini, M. Begon, M. Lévesque, Numerical homogenization of a linearly elastic honeycomb lattice structure and comparison with analytical and experimental results, *Mech. Mater.* 167 (2022) 104210, <https://doi.org/10.1016/j.mechmat.2022.104210>, <https://www.sciencedirect.com/science/article/pii/S0167663622000011>.
- [62] C. Geuzaine, J.-F. Remacle, Gmsh: a 3-D finite element mesh generator with built-in pre- and post-processing facilities, *Int. J. Numer. Methods Eng.* 79 (11) (2009) 1309–1331, <https://doi.org/10.1002/nme.2579>, <https://onlinelibrary.wiley.com/doi/abs/10.1002/nme.2579>.
- [63] G. Dhondt, *The Finite Element Method for Three-Dimensional Thermomechanical Applications*, [elektronische ressource] Edition, Wiley, Chichester [u.a.], 2004, differences between the printed and electronic version of the document are possible <https://api.semanticscholar.org/CorpusID:117913376>.
- [64] R.D. Mindlin, Micro-structure in linear elasticity, *Arch. Ration. Mech. Anal.* 16 (1) (1964) 51–78, <https://doi.org/10.1007/BF00248490>.
- [65] R. Mindlin, Second gradient of strain and surface-tension in linear elasticity, *Int. J. Solids Struct.* 1 (4) (1965) 417–438, [https://doi.org/10.1016/0020-7683\(65\)90006-5](https://doi.org/10.1016/0020-7683(65)90006-5), <https://linkinghub.elsevier.com/retrieve/pii/0020768365900065>.
- [66] V. Kouznetsova, M.G.D. Geers, W.a.M. Brekelmans, Multi-scale constitutive modelling of heterogeneous materials with a gradient-enhanced computational homogenization scheme, *Int. J. Numer. Methods Eng.* 54 (8) (2002) 1235–1260, <https://doi.org/10.1002/nme.541>, <https://onlinelibrary-wiley-com.ezproxy.biblio.polito.it/doi/abs/10.1002/nme.541>.
- [67] V. Kouznetsova, M. Geers, W. Brekelmans, Multi-scale second-order computational homogenization of multi-phase materials: a nested finite element solution strategy, *Comput. Methods Appl. Mech. Eng.* 193 (48–51) (2004) 5525–5550, <https://doi.org/10.1016/j.cma.2003.12.073>, <https://linkinghub.elsevier.com/retrieve/pii/S0045782504002853>.
- [68] O. Weeger, Numerical homogenization of second gradient, linear elastic constitutive models for cubic 3D beam-lattice metamaterials, *Int. J. Solids Struct.* 224 (2021) 111037, <https://doi.org/10.1016/j.ijsolstr.2021.03.024>, <https://www.sciencedirect.com/science/article/pii/S0020768321001153>.
- [69] I.A. Rodrigues Lopes, F.M. Andrade Pires, Unlocking the potential of second-order computational homogenisation: an overview of distinct formulations and a guide for their implementation, *Arch. Comput. Methods Eng.* 29 (3) (2022) 1339–1393, <https://doi.org/10.1007/s11831-021-09611-9>.
- [70] W.F. Dos Santos, I.A. Rodrigues Lopes, F.M. Andrade Pires, S.P. Proença, Exploring novel mechanical metamaterials: unravelling deformation mode coupling and size effects through second-order computational homogenisation, *Int. J. Solids Struct.* 292 (2024) 112724, <https://doi.org/10.1016/j.ijsolstr.2024.112724>, <https://linkinghub.elsevier.com/retrieve/pii/S0020768324000817>.
- [71] C. Miehe, A. Koch, Computational micro-to-macro transitions of discretized microstructures undergoing small strains, *Arch. Appl. Mech.* 72 (4) (2002) 300–317, <https://doi.org/10.1007/s00419-002-0212-2>.
- [72] D. Li, W. Liao, N. Dai, Y.M. Xie, Comparison of mechanical properties and energy absorption of sheet-based and strut-based gyroid cellular structures with graded densities, *Materials* 12 (13) (2019) 2183, <https://doi.org/10.3390/ma12132183>, <https://www.mdpi.com/1996-1944/12/13/2183>.
- [73] R.K. Abu Al-Rub, D.-W. Lee, K.A. Khan, A.N. Palazotto, Effective anisotropic elastic and plastic yield properties of periodic foams derived from triply periodic Schoen's I-WP minimal surface, *J. Eng. Mech.* 146 (5) (2020) 04020030, [https://doi.org/10.1061/\(ASCE\)EM.1943-7889.0001759](https://doi.org/10.1061/(ASCE)EM.1943-7889.0001759), <https://ascilibrary.org/doi/10.1061/%28ASCE%29EM.1943-7889.0001759>.
- [74] S. Hazanov, C. Huet, Order relationships for boundary conditions effect in heterogeneous bodies smaller than the representative volume, *J. Mech. Phys. Solids* 42 (12) (1994) 1995–2011, [https://doi.org/10.1016/0022-5096\(94\)90022-1](https://doi.org/10.1016/0022-5096(94)90022-1), <https://www.sciencedirect.com/science/article/pii/0022509694900221>.
- [75] M. Hori, S. Nemat-Nasser, On two micromechanics theories for determining micro-macro relations in heterogeneous solids, *Mech. Mater.* 31 (10) (1999) 667–682, [https://doi.org/10.1016/S0167-6636\(99\)00020-4](https://doi.org/10.1016/S0167-6636(99)00020-4), <https://www.sciencedirect.com/science/article/pii/S0167663699000204>.
- [76] Z. Xia, C. Zhou, Q. Yong, X. Wang, On selection of repeated unit cell model and application of unified periodic boundary conditions in micro-mechanical analysis of composites, *Int. J. Solids Struct.* 43 (2) (2006) 266–278, <https://doi.org/10.1016/j.ijsolstr.2005.03.055>, <https://www.sciencedirect.com/science/article/pii/S0020768305001460>.
- [77] F.J.P. Reis, F.M. Andrade Pires, A mortar based approach for the enforcement of periodic boundary conditions on arbitrarily generated meshes, *Comput. Methods Appl. Mech. Eng.* 274 (2014) 168–191, <https://doi.org/10.1016/j.cma.2014.01.029>, <https://www.sciencedirect.com/science/article/pii/S0045782514000528>.
- [78] O. Ouchetto, S. Zaamoun, Periodic boundary conditions in the FEM using arbitrary meshes, in: 2016 21st International Conference on Microwave, Radar and Wireless Communications (MIKON), 2016, pp. 1–3.
- [79] O. Ouchetto, B. Essakhi, S. Jai-Andaloussi, S. Zaamoun, Handling periodic boundary conditions on arbitrary mesh, *IET Microw. Antennas Propag.* 12 (8) (2018) 1266–1272, <https://doi.org/10.1049/iet-map.2017.0870>, <https://onlinelibrary.wiley.com/doi/abs/10.1049/iet-map.2017.0870>.
- [80] D. Garoz, F. Gilabert, R. Sevenois, S. Spronk, W. Van Paepegem, Consistent application of periodic boundary conditions in implicit and explicit finite element simulations of damage in composites, *Composites, Part B, Eng.* 168 (2019) 254–266, <https://doi.org/10.1016/j.compositesb.2018.12.023>, <https://linkinghub.elsevier.com/retrieve/pii/S1359836818337776>.
- [81] J. Wippler, S. Fünfschilling, F. Fritzen, T. Böhlke, M.J. Hoffmann, Homogenization of the thermoelastic properties of silicon nitride, *Acta Mater.* 59 (15) (2011) 6029–6038, <https://doi.org/10.1016/j.actamat.2011.06.011>, <https://www.sciencedirect.com/science/article/pii/S1359645411004162>.
- [82] R. Shashidhar Reddy, S. Panda, The energy-based method for effective dynamic properties of viscoelastic composite, *Mater. Today Proc.* 18 (2019) 4190–4200, <https://doi.org/10.1016/j.matpr.2019.07.364>, <https://linkinghub.elsevier.com/retrieve/pii/S221478531932543X>.